Economic Geology, v. 116, no. 8, pp. 1803–1824

Diagenetic Controls on the Formation of the Anarraaq Clastic-Dominated Zn-Pb-Ag Deposit, Red Dog District, Alaska

Merilie A. Reynolds,[1,†] Sarah A. Gleeson,[2,3] Robert A. Creaser,[4] Betsy A. Friedlander,[5] Jenny C. Haywood,[5] Danny Hnatyshin,[6,7] Jim McCusker,[5] and John W.F. Waldron[4]

[1]*Northwest Territories Geological Survey, Government of Northwest Territories, Yellowknife, Canada*

[2]*GFZ German Research Centre for Geosciences, 14473 Potsdam, Germany*

[3]*Institute of Geological Sciences, Freie Universität Berlin, Malteserstrasse 74-100, Berlin 12249, Germany*

[4]*Department of Earth and Atmospheric Sciences, University of Alberta, Edmonton, Alberta T6G 2E3, Canada*

[5]*Teck Resources Limited, Suite 3300, Bentall 5, 550 Burrard Street, Vancouver, British Columbia V6C 0B3, Canada*

[6]*Irish Centre for Research in Applied Geosciences (iCRAG), University College Dublin, Belfield, Dublin 4, Ireland*

[7]*UCD School of Earth Sciences, University College Dublin, Belfield, Dublin 4, Ireland*

Abstract

The Anarraaq clastic-dominated (CD) Zn-Pb-Ag deposit (Red Dog district, Alaska, USA) has an inferred mineral resource of 19.4 Mt at 14.4% Zn, 4.2% Pb, and 73 g/t Ag and is spatially associated with a separate ~1 Gt barite body. This study presents new cross sections and petrographic evidence from the Anarraaq area. The barite body, previously shown to have formed in a shallow subsurface environment akin to a methane cold seep, contains multiple generations of barite with locally abundant calcite masses, which are discordant to sedimentary laminae, and is underlain by an interval of massive pyrite containing abundant framboids and radiolarians. Calcite and pyrite are interpreted to have formed by methane-driven diagenetic alteration of host sediment at the sulfate-methane transition (SMT). The sulfide deposit contains two zones of Zn-Pb mineralization bounded by faults of unknown displacement. The dominant hydrothermal minerals are marcasite, pyrite, sphalerite, quartz, and galena. The presence of hydrothermal pseudomorphs after barite, early pyrite resembling diagenetic pyrite associated with the barite body, and hydrothermal quartz and sphalerite filling voids formed by dissolution of carbonate all suggest that host sediment composition and origin was similar to that of the barite body prior to hydrothermal mineralization. Rhenium-osmium isochron ages of Ikalukrok mudstone (339.1 ± 8.3 Ma), diagenetic pyrite (333.0 ± 7.4 Ma), and hydrothermal pyrite (334.4 ± 5.3 Ma) at Anarraaq are all within uncertainty of one another and of an existing isochron age (~338 Ma) for the Main deposit in the Red Dog district. This indicates that the Anarraaq deposit formed soon after sedimentation and that hydrothermal activity was approximately synchronous in the district. The initial Os composition of the Anarraaq isochrons (0.375 ± 0.019–0.432 ± 0.025) is consistent with contemporaneous seawater, indicating that a mantle source was not involved in the hydrothermal system. This study highlights the underappreciated but important role of early, methane-driven diagenetic processes in the paragenesis of some CD deposits and has important implications for mineral exploration.

Introduction

The Red Dog district in northwestern Alaska contains several world-class clastic-dominated (CD) Zn-Pb deposits (Fig. 1; Blevings et al., 2013). CD Zn-Pb deposits are a subtype of sediment-hosted massive sulfide (SHMS) deposits that are hosted in carbonaceous mudstone (Leach et al., 2010); this type of deposit has traditionally been referred to as sedimentary exhalative (SEDEX; Goodfellow et al., 1993). Within the Red Dog district, the Anarraaq sulfide deposit contains an inferred mineral resource of 19.4 Mt at 14.4% Zn, 4.2% Pb, and 73.4 ppm Ag (Krolak et al., 2017). Barite and Fe sulfide (pyrite and marcasite) are common components of the Red Dog CD deposits. Importantly, barite produces a strong gravity anomaly that has proven to be a powerful tool in exploration of the district (Blevings et al., 2013). However, barite and Zn-Pb-Fe sulfides also occur independent of each other in the district, and Fe sulfide is the dominant component in some low-grade Zn-Pb prospects in the Red Dog district (Fig. 1; Kelley and Jennings, 2004; Blevings et al., 2013). The genetic controls on the varying relationships of these components are not well understood.

The Anarraaq area of the Red Dog district is an ideal place to investigate the relationships between diagenetic and hydrothermal processes because it contains a sulfide-only deposit and a barite-only body (Kelley et al., 2004b), and recent drilling allows good geologic control. The Anarraaq barite body could contain as much as 1 Gt of barite and is separated from the sulfide deposit below by 20–60 m of barren host rock (Kelley et al., 2004b). Kelley et al. (2004b, p. 1586) reported only rare barite in the Anarraaq sulfide deposit or in laterally equivalent strata, concluding that it was "unlikely that the sulfides replaced barite." They instead interpret sulfides to have replaced sedimentary carbonate layers within the mudstone (Kelley et al., 2004b).

In this study, we present new cross sections and petrographic data from the Anarraaq barite body and the Anarraaq sulfide deposit and document the distribution of the major

[†]Corresponding author: e-mail, Merilie_Reynolds@gov.nt.ca

© 2021 Gold Open Access: This paper is published under the terms of the CC-BY-NC license.

ISSN 0361-0128; doi:10.5382/econgeo.4849; 22 p.
Digital appendices are available in the online Supplements section.

Submitted: February 18, 2019 / Accepted: February 8, 2021

Downloaded from http://pubs.geoscienceworld.org/segweb/economicgeology/article-pdf/116/8/1803/5428899/4849_reynolds_et_al.pdf
by Freie Universitaet Berlin user

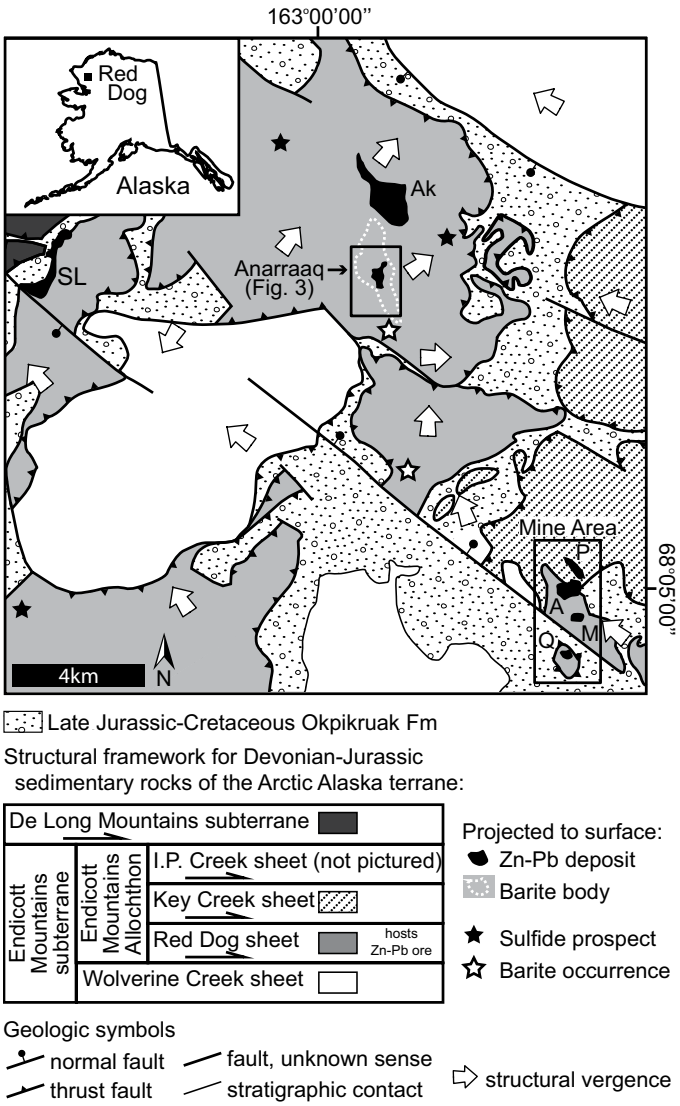

Fig. 1. Regional map of thrust sheets in the Red Dog district. Modified after figures 2, 3, and 14 in Blevings et al. (2013). Mine area deposits include Main (M), Aqqaluk (A), Paalaaq (P), and Qanaiyaq (Q). Other deposits include Anarraaq, Aktigiruk (Ak), and Su Lik (SL). Several additional prospects and barite occurrences are also highlighted.

paragenetic components on the deposit scale. We also present the first paragenetic scheme for the deposit that includes both sulfide and gangue minerals and show that hydrothermal sulfide mineralization did replace diagenetic barite. Finally, rhenium-osmium isotope geochemistry is used to constrain the age of the Anarraaq sulfide deposit relative to host sediment, diagenetic alteration, and other Red Dog deposits.

Regional Geology

The Red Dog district is in the Arctic Alaska terrane, which comprises Devonian to Jurassic sedimentary rocks deposited on a passive continental margin (Moore et al., 1986, 1994). The area underwent significant shortening during the Late Jurassic to Cretaceous Brookian orogeny, when the terrane collided with an intraoceanic island arc (Moore et al., 1986, 1994). District geology is characterized by thrusts, folds, and very low grade metamorphism (De Vera et al., 2004). The region has been divided into multiple fault-bounded and age-equivalent allochthons and structural plates (referred herein as sheets; Fig. 1; Young, 2004; Blevings et al., 2013). All known CD deposits in the Red Dog district are hosted in the Red Dog thrust sheet of the Endicott Mountains allochthon (Figs. 1, 2; Blevings et al., 2013). In the Anarraaq area, structural vergence is to the northeast (Fig. 1; De Vera, 2005), and thrust faults are offset by steeply dipping tear faults that accommodate variable lateral displacement (Fig. 3; Blevings et al., 2013).

The Red Dog CD deposits are hosted in the Ikalukrok unit, which makes up the upper part of the Mississippian Kuna Formation and is the deep-water facies of the Lisburne Group (Dumoulin et al., 2004). The Kuna Formation was deposited in a sediment-starved, extensional basin flanked by carbonate platforms (Young, 2004). The Ikalukrok unit primarily comprises black biosiliceous mudstone and chert with locally abundant intercalations of carbonate and barite (Dumoulin et al., 2004; Johnson et al., 2004) and cut by igneous intrusions linked to extensional and transtensional deformation (Young, 2004). Rocks of the Ikalukrok unit are characterized by high concentrations of organic carbon, silicon, and phosphate, with abundant radiolarians (Dumoulin et al., 2004, 2014; Slack et al., 2004). Upwelling of nutrient-rich waters played an important role in the regional depositional regime (Dumoulin et al., 2014) and may have given rise to a fluctuating oxygen minimum zone that resulted in variable redox conditions (Reynolds et al., 2015). Carbonate layers in the Ikalukrok can be up to 40 m thick and up to 80 m in cumulative thickness and are generally thought to originate from the erosion of adjacent carbonate platforms (Dumoulin et al., 2004). The abundance of calcareous mass flow deposits in the Ikalukrok increases from south to north and is relatively high at Anarraaq (Dumoulin et al., 2004).

The model for Red Dog CD Zn-Pb mineralization calls for a saline brine (14–19 wt % NaCl equiv) that originated from evaporated seawater and was heated to 100°–200°C as it circulated in the subsurface (Leach et al., 2004). The source of metals is inferred to be the fluvial-deltaic sandstones and conglomerates of the Devonian Endicott Group below the Kuna Formation (Young, 2004). The hydrothermal fluid ascended to the surface via extensional faults; some sulfides were deposited in shallow muds or replaced barite (e.g., mine area deposits; Kelley et al., 2004a), and some replaced calcareous mass flow deposits within the Ikalukrok unit (e.g., Anarraaq deposit, Kelley et al., 2004b). Hydrothermal pyrite in the Main deposit was dated at 338.3 ± 5.8 Ma (Re-Os), which is coeval, within uncertainty, to the biostratigraphic age of the upper Kuna Formation (Morelli et al., 2004).

Anarraaq

Kelley et al. (2004b) provide an excellent descriptive overview of the Anarraaq area. In brief, the Anarraaq sulfide deposit is a lenticular body located ~650 m below the surface. The highest grades (20–30% Zn) occur in the southeastern part of the deposit, which is inferred to have formed near a Carboniferous extensional fault that acted as the primary conduit for hydrothermal fluids, although no such fault has been identified. The northwestern part of the deposit is characterized by >60% pyrite and marcasite with minor amounts of base metal sulfide. To explain the size and shape of the sulfide body and

Downloaded from http://pubs.geoscienceworld.org/segweb/economicgeology/article-pdf/116/8/1803/5428899/4849_reynolds_et_al.pdf
by Freie Universitaet Berlin user

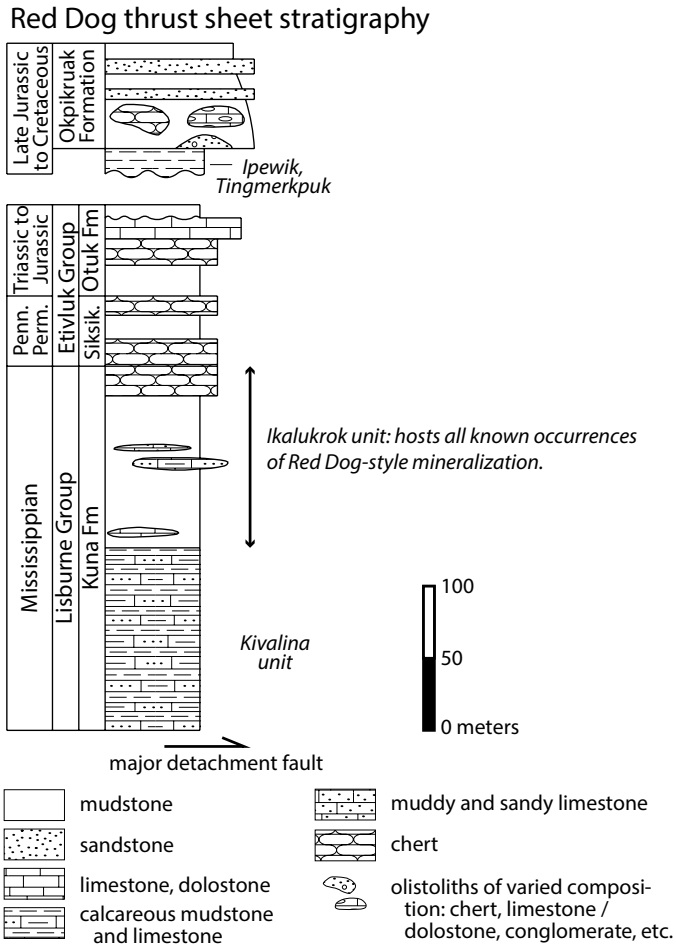

Fig. 2. Generalized stratigraphy of the Red Dog thrust sheet, which hosts all known clastic-dominated Zn-Pb mineralization in the Red Dog district. Modified after figure 4 in Blevings et al. (2013).

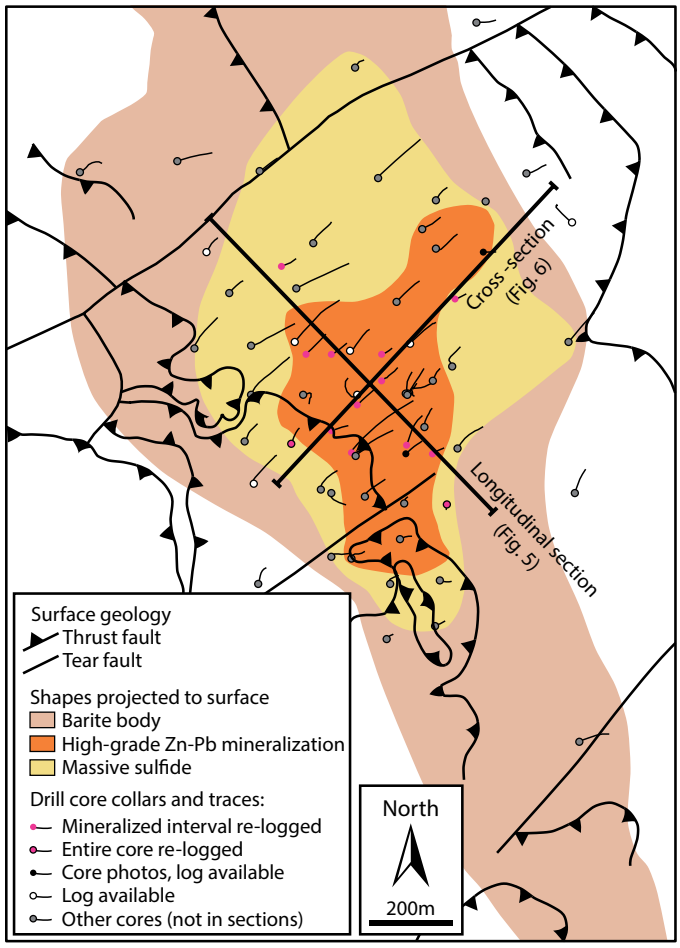

Fig. 3. Plan map of the Anarraaq area. Modified after figure 14 in Blevings et al. (2013). The high-grade Zn-Pb mineralization shape indicates grade thickness ≥140 Zn + Pb% × m (S.K. Blevings, pers. commun., 2019).

some sulfide textures, Kelley et al. (2004b) suggested that the mineralizing fluids preferentially replaced calcareous mass flows deposited in a submarine channel. The sulfide body is underlain by a basal fault and may be separated from overlying strata by a thrust fault.

The strata overlying the sulfide deposit contains a 9- to 67-m lower interval of mudstone with disseminated sulfides that extend up to 20 m above the sulfide deposit, 10–20 m of mudstone interbedded with calcareous mass flow deposits (i.e., lithic turbidite and calcareous radiolarite), 10–20 m of black mudstone, and 10–20 m of chert and calcareous radiolarite. Above that, the Anarraaq barite body ranges in thickness from 65 to 140 m; some parts may have been structurally thickened. The barite body consists of a lower zone of massive, laminated barite, the basal part of which is variably calcareous, and an upper zone of nodular barite in black chert and mudstone. The barite body is overlain by younger strata with multiple repeating thrust sheets verging northeast.

Methane-Driven Diagenetic Processes

Barite in the Red Dog district is thought to have formed when diagenetic fluids enriched in methane and barium vented into sulfate-bearing bottom waters or shallow pore waters (Ayuso et al., 2004; Johnson et al., 2004, 2009). This type of environment is analogous to cold methane seeps (Suess, 2014). Baritic cold methane seeps generally form on continental margins with abundant biogenic productivity in the overlying water column (Torres et al., 2003). In such settings, biologically mediated barite precipitation in the water column results in relatively high concentrations of biogenic barite in organic-rich, and commonly opal-rich, sediment (Bishop, 1988; Paytan et al., 1993). Degradation of organic matter during burial creates strongly reducing, methane-rich pore waters that dissolve the biogenic barite (Brumsack, 1986; Torres et al., 1996). Where these fluids migrate into sulfate-bearing seawater or shallow pore waters, barite reprecipitates (Brumsack, 1986; Torres et al., 1996, 2003).

Because barium is transported in methane-bearing fluids, barite precipitation is closely linked to an important biological process: sulfate driven-anaerobic oxidation of methane (SD-AOM), which proceeds by reaction 1 (Barnes and Goldberg, 1976; Reeburgh, 1976):

$$CH_4 + SO_4^{2-} \rightarrow HCO_3^- + HS^- + H_2O. \quad (1)$$

Downloaded from http://pubs.geoscienceworld.org/segweb/economicgeology/article-pdf/116/8/1803/5428899/4849_reynolds_et_al.pdf
by Freie Universitaet Berlin user

This reaction is mediated by a consortium of sulfate-reducing bacteria and syntrophic anaerobic methanotrophic archea (Hoehler et al., 1994; Knittel and Boetius, 2009). Sulfate-driven anaerobic oxidation of methane commonly takes place below the sediment surface in a zone called the sulfate-methane transition (SMT; Fig. 4; Iversen and Jørgensen, 1985). There, upward-diffusing methane and downward-diffusing seawater sulfate are depleted by SD-AOM (Iversen and Jørgensen, 1985). Diagenetic barite precipitates just above the SMT (Dickens, 2001), where the absence of methane and the presence of sulfate result in a decrease in the solubility of barium. SD-AOM is also associated with the precipitation of authigenic carbonate (e.g., Paull et al., 1992) and pyrite (e.g., Lin, Q., et al., 2016; Lin, Z., et al., 2016). However, at Anarraaq, authigenic carbonate associated with the barite bed has not been identified previously (Johnson et al., 2004).

At Red Dog, Kelley et al. (2004a) proposed that thermogenic reductive dissolution of early barite provided an important source of S for later hydrothermal sulfide mineralization in the mine area deposits (Qanaiyaq, Main, Aqqaluk, and Paalaaq; Fig. 1). Furthermore, Johnson et al. (2004) recognized the link between barite precipitation and SD-AOM as a possible source of reduced sulfide (HS^-) for formation of Zn-Pb mineralization. The barite body at Anarraaq is not overprinted by Zn-Pb mineralization and, therefore, provides insight into how methane-driven diagenetic processes altered the host sediment before the hydrothermal system developed. As such, it is an ideal study site to assess the role that diagenetic processes may play in the development of the hydrothermal system.

Methods

Relogging and thin-section petrography

The petrographic observations reported in this study are drawn from the detailed relogging of 13 drill cores along two sections through the Anarraaq area (Fig. 3), >500 samples of cut core, and >80 thin sections (locations shown on Figs. 5, 6). Cores were painted with a dilute HCl solution containing alizarin red S and potassium ferricyanide to allow rapid identification of carbonate minerals (Hitzman, 1999). In addition to detailed hand sample and thin-section petrographic descriptions, the scanning electron microscope (SEM) at the University of Alberta was used to confirm mineralogy and microscopic textural relationships with dispersive spectroscopy (EDS) and backscattered electron (BSE) imaging. Spot checks using micro-Raman spectroscopy were used to verify visual identification of pyrite and marcasite. Additional lithological and textural details were drawn from original logs and high-resolution photographs of fresh core.

Re-Os sampling and analytical methods

Three samples from drill core were used for Re-Os analyses (Fig. 5A). Sample 923-2123 is 30 cm of core composed of black mudstone with disseminated pyrite and minor quartz-calcite veinlets (App. Fig. A1A) and located approximately 12 m above the Anarraaq sulfide deposit. Veinlets and macroscopic accumulations of pyrite were avoided during sampling of mudstone. Sample 1716-2520.8 is 20 cm of core that consists of visibly unmineralized mudstone with diagenetic pyrite nodules from the Anarraaq sulfide deposit (App. Fig. A1B). The pyrite nodules are crosscut by minor quartz veinlets, which were excluded during sampling. Sample 1723-2104.5 is 20 cm of core that comprises hydrothermal pyrite enclosed in calcite (App. Fig. A1C).

The Re-Os analyses were carried out at the Crustal Re-Os Geochronology Laboratory of the Department of Earth and Atmospheric Sciences, University of Alberta, Canada. Each sample was cut from original core material using a rock saw and then polished to remove any residue. Mudstone samples were then powdered in an agate mill, whereas pyrite samples were manually crushed using ceramics to a size of approximately 1–5 mm and handpicked under a stereoscope to remove any impurities. Several hundred milligrams of sample were then added to a Carius tube with a known amount of ^{185}Re and ^{190}Os spike solution and 8 mL of CrO_3-H_2SO_4 (for mudstones) or 2 mL of 10 N HCl and 6 mL 16 N HNO_3 (for pyrite). The Carius tubes were sealed and heated to 220°C for 48 (pyrite) to 72 h (mudstone) to ensure sample-spike equilibration. Additional details of the chemical procedures for sample digestion and purification of Re and Os are provided by Selby and Creaser (2003) and Hnatyshin et al. (2016).

The abundance and isotopic composition of Re and Os were determined by isotope dilution-negative thermal ionization mass spectrometry (ID-NTIMS) with a ThermoScientific Triton NTIMS under conditions comparable to those of Hnatyshin et al. (2016) to ensure a stable ion beam. Data were reduced according to the method of Kendall et al. (2004),

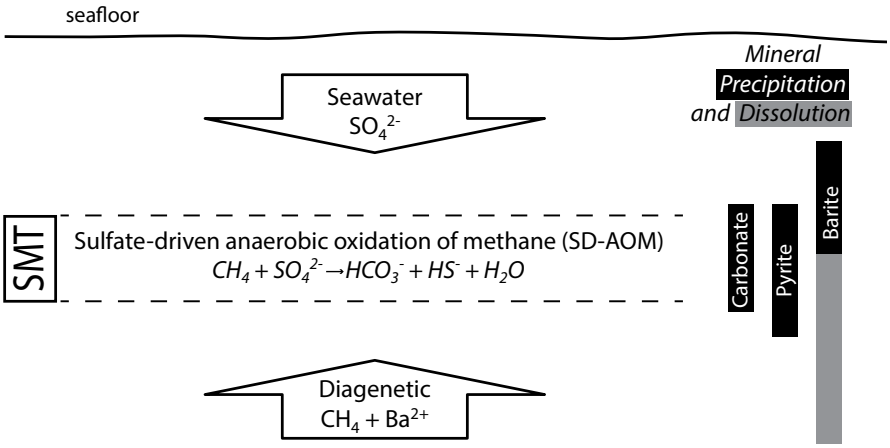

Fig. 4. The sulfate methane transition (SMT) forms where downward-diffusing seawater sulfate and upward-diffusing methane are depleted via sulfate-driven anaerobic oxidation of methane. This reaction can result in the precipitation of carbonate and pyrite. Barite is soluble in the methanic pore waters below the SMT but not above.

Downloaded from http://pubs.geoscienceworld.org/segweb/economicgeology/article-pdf/116/8/1803/5428899/4849_reynolds_et_al.pdf
by Freie Universitaet Berlin user

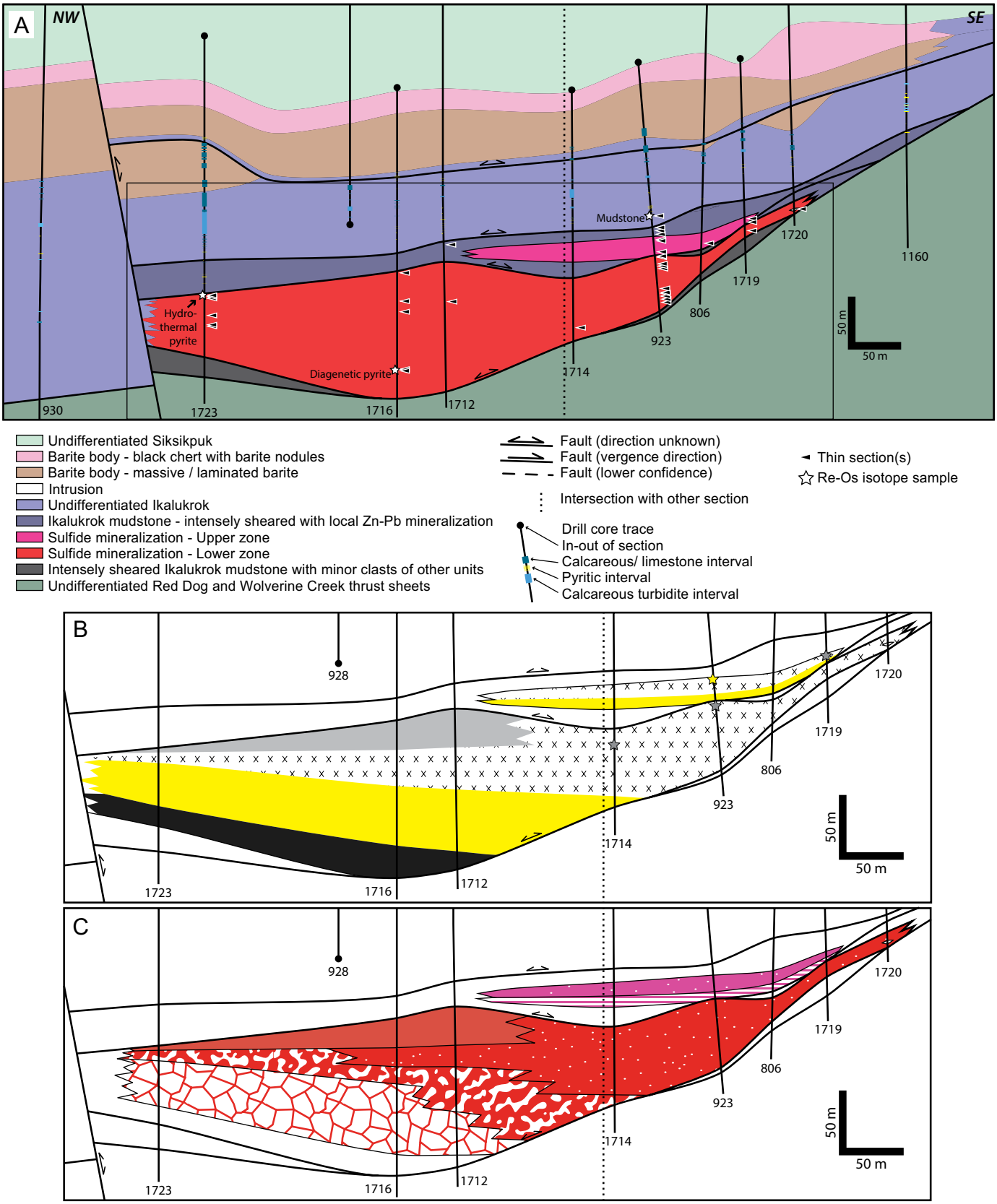

Fig. 5. (A) Longitudinal section through the central part of the Anarraaq sulfide deposit, oriented perpendicular to the direction of transport during Brookian shortening. Inset shows (B) spatial distribution of diagenetic components and (C) hydrothermal mineralization styles. See additional legend items in Figure 6.

Downloaded from http://pubs.geoscienceworld.org/segweb/economicgeology/article-pdf/116/8/1803/5428899/4849_reynolds_et_al.pdf
by Freie Universitaet Berlin user

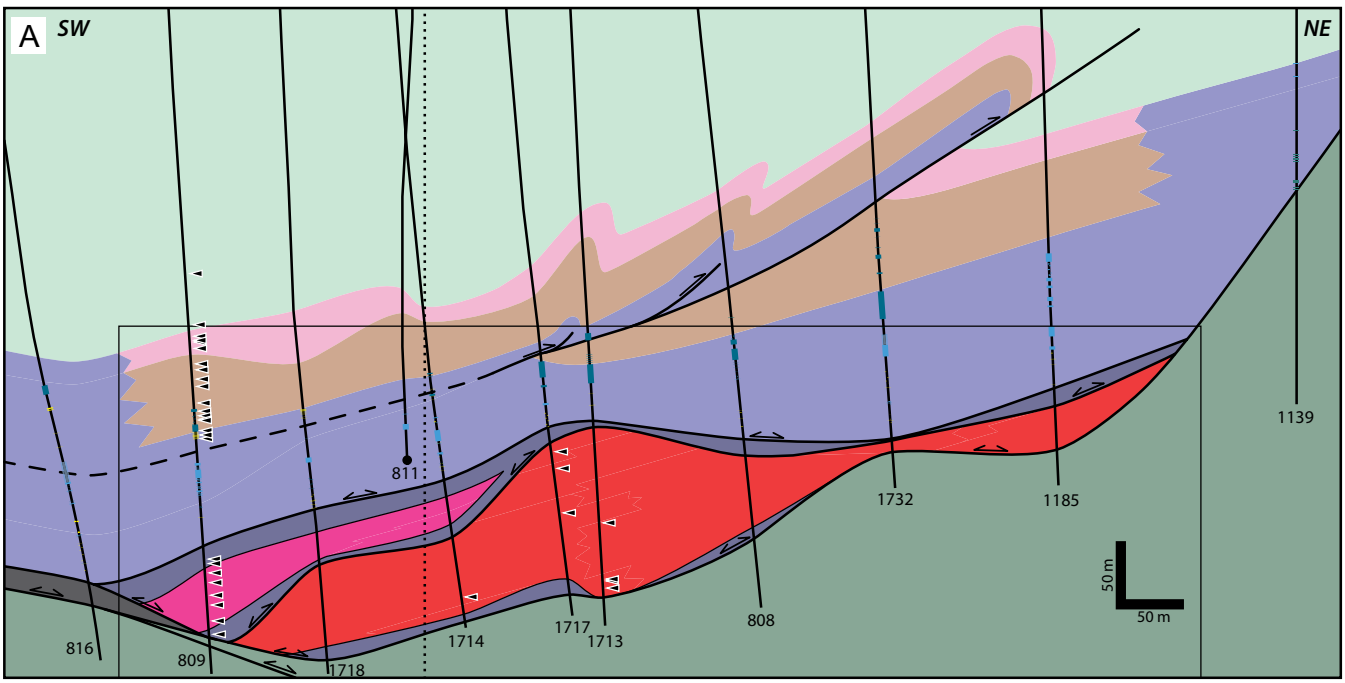

Dominant diagenetic components

- Barite (altered to quartz and sulfides) in black mudstone
- Poorly preserved host
- Fe sulfide layers, nodules >20% in black mudstone
- Fe sulfides layers, nodules <20% in black mudstone
- Barite identified in single sample
- Layers of tightly packed framboids identified in single sample

Dominant mineralized textures

Upper zone
- Widespread massive sulfide
- Laminated sphalerite

Lower zone
- Preferential replacement of barite by Zn-Pb mineralization
- Widespread Zn-Pb mineralized breccia
- Zn-Pb mineralized breccia interspersed with intervals of mudstone
- Sphalerite veining

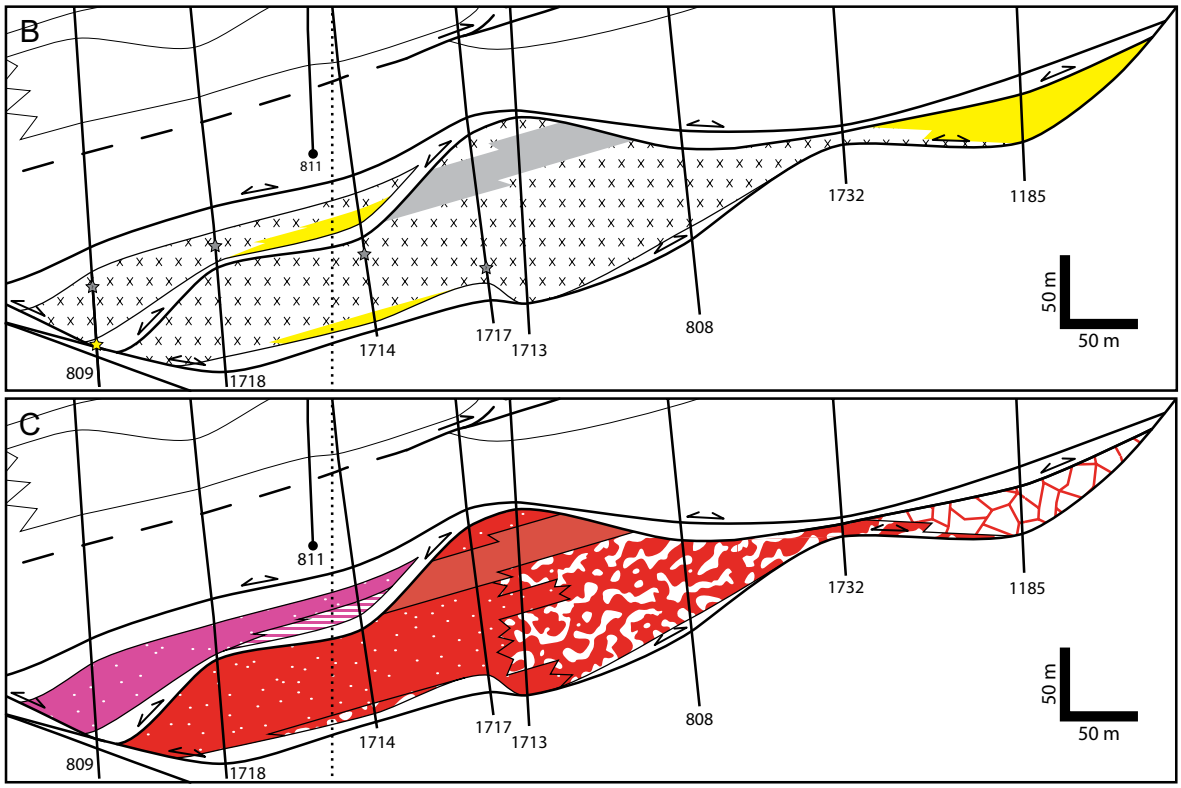

Fig. 6. (A) Cross section through the central part of the Anarraaq sulfide deposit, oriented parallel to the inferred direction of transport during Brookian shortening (to the northeast). Inset shows spatial distribution of (B) diagenetic components and (C) hydrothermal mineralization styles. Additional legend items in Figure 5.

Downloaded from http://pubs.geoscienceworld.org/segweb/economicgeology/article-pdf/116/8/1803/5428899/4849_reynolds_et_al.pdf
by Freie Universitaet Berlin user

whereby 2σ uncertainties for $^{187}Re/^{188}Os$ and $^{187}Os/^{188}Os$ are determined by numerical error propagation and implementation of an error correlation (ρ) between $^{187}Re/^{188}Os$ and $^{187}Os/^{188}Os$. Blank corrections for mudstone data were 0.3 ± 0.1 pg for Os at a ^{187}Os-^{188}Os ratio of 0.20 ± 0.05 and 15 ± 3 pg for Re. For pyrite, the Os blank correction is 0.047 ± 0.012 pg at a ^{187}Os-^{188}Os ratio of 0.183 ± 0.056, the Re correction being 1.1 ± 0.6 pg. Age calculations of Re-Os isotope data were performed using Isoplot version 3.00 (Ludwig, 2001) and the ^{187}Re decay constant of Smoliar et al. (1996).

Results

Cross sections

Figures 5 and 6 show new cross sections constructed by correlating logs parallel to, and transverse to, the inferred thrust transport direction. Two discrete zones of sulfide mineralization can be distinguished: the Lower zone and the Upper zone (Figs. 5, 6). The mineralized zones are characterized by distinctive styles of Zn-Pb mineralization (see below for more details) and are bounded by intervals of sheared mudstone that contain local sulfide-bearing fragments. The boundaries of these shear zones are marked as faults in Figures 5 and 6, but the magnitude of displacement along them is poorly constrained.

The interval of unmineralized Ikalukrok between the barite body and the sulfide deposit ranges from <50 m in the center of the deposit to >100 m in the northeast (Fig. 6A). The calcareous turbidite is broadly continuous across both sections. Whereas the turbidite unit is typically ~20 m thick, it can be as thin as a 2-m interval of calcareous sandstone or ~10 m of mudstone with minor micrite layers <10 cm in the central and southeastern parts of the area. Carbonate in the lower part of the barite body and in the underlying mudstone is discontinuous. The combined maximum thickness of the calcareous beds encountered in this study is 50 m in core 1723.

At least one thrust fault cuts upsection through the Anarraaq barite body. Evidence for fault-related folding in the hanging wall includes changes in unit thickness and bedding oriented at a low angle to the core axis. Additional structures may be responsible for other variations in stratigraphic thickness of the massive and nodular barite units.

The petrographic features of the barite body and sulfide deposit are described in the following section.

Hand specimen descriptions, petrography, and paragenesis

The Anarraaq barite body and sulfide deposit contain dark-colored, fine-grained, noncalcareous rocks with variable fissility and hardness. In this study, these rocks are referred to as mudstone. If conchoidal fracture is observed in hand specimen or microcrystallinity in thin section, the term "chert" is used instead, but these distinguishing features are difficult to identify in small domains of mudstone within zones of massive barite/sulfide or where abundant organic material obscures the texture in thin section. More detailed descriptions of the sedimentary rocks of the Ikalukrok can be found in Dumoulin et al. (2004), Kelley et al. (2004a), and Slack et al. (2004).

Barite body: The barite body is well described by Kelley et al. (2004b); we note some additional detailed observations. In thin section, samples of massive, laminated barite typically containing chert with variable organic content and disseminated to patchy barite (Fig. 7B, C). The grain size of the barite is ≤30 μm and the crystal boundaries are highly irregular to embayed, suggesting dissolution and remobilization (Fig. 7F). Calcareous intervals are not strongly laminated but still commonly contain some chert (Fig. 7D, E). Locally the boundaries between calcite-rich and chert-rich domains crosscut remnant sedimentary laminae (Fig. 7E). Calcite also contains distinctive barite laths ~20 μm in length that appear to have been preserved from dissolution (Fig. 7G). Radiolarians are commonly preserved as spheres of chalcedony or coarser crystalline barite (~50 μm) or as spheres of calcite in the calcareous zones (Fig. 7). Massive cryptocrystalline barite clearly crosscuts cherty and calcareous baritic zones (Fig. 7A), suggesting it formed by replacing the latter.

Veins of coarsely crystalline barite are ubiquitous in the Anarraaq barite body. In some places, these veins are clearly associated with a local increase in the abundance of disseminated barite in the surrounding host rock (Fig. 7B). Barite veins commonly contain patches of pyrobitumen enclosing euhedral barite crystals (Figs. 7H) and rare calcite.

In several drill cores, an interval of bedded to nodular pyrite (≤6 m thick) occurs just below the massive barite (Figs. 5, 6). Pyrite beds consist of abundant framboids and spheroids, which are enclosed by a later generation of massive fine-crystalline pyrite (Fig. 8A-D). Abundant siliceous skeletal material is preserved in the massive pyrite, including local radiolarians that are essentially intact (Fig. 8B, C). A minor later generation of cubic pyrite is associated with crosscutting quartz veinlets.

Sulfide deposit—Lower zone: Host strata of the Lower zone contain diagenetic barite and pyrite, lesser marcasite, and rare apatite laths that predate Zn-Pb mineralization (Fig. 9). Evidence for barite is present in the form of pseudomorphs after discrete laths (generally ≤200 μm but locally >1 cm) and nodules and layers composed of laths that coalesce into amorphous masses (Fig. 10A, B). Although most barite is completely replaced by quartz (Fig. 10C) or sphalerite (Fig. 10D, E), rare barite has been detected by EDS (Fig. 10E). Diagenetic Fe sulfide occurs disseminated in mudstone and as macroscopic layers, laminae, and nodules (e.g., Fig. 8I). In hand sample, early Fe sulfides are very finely crystalline and relatively dull in luster. Nodules are several millimeters to 10 cm in diameter and range from rounded to subangular, tabular to irregular. Layers are commonly 1 cm thick or less. Nodules and layers locally coalesce such that up to a meter of core may be massive Fe sulfide. Pyrite occurs as framboids (Fig. 8F) or spheroids (Fig. 8G), euhedral crystals that locally overgrow framboids (Fig. 8F), and fine crystalline masses (Fig. 8F-H) that are locally intergrown with slightly coarser marcasite. A distinctive characteristic of the early Fe sulfide is the abundance of siliceous inclusions, many of which are clearly biogenic in origin. The best-preserved microfossils are radiolarians (Fig. 8G, H) and the morphology of less complete skeletal fragments is mostly consistent with this identification.

The host strata in the Lower zone are best preserved in the three cores in the northwestern half of the longitudinal section (cores 1723, 1716, and 1712; Fig. 5A) where overprinting by hydrothermal mineralization is the least destructive of preexisting textures. These cores show a consistent stratigraphic

Downloaded from http://pubs.geoscienceworld.org/segweb/economicgeology/article-pdf/116/8/1803/5428899/4849_reynolds_et_al.pdf
by Freie Universitaet Berlin user

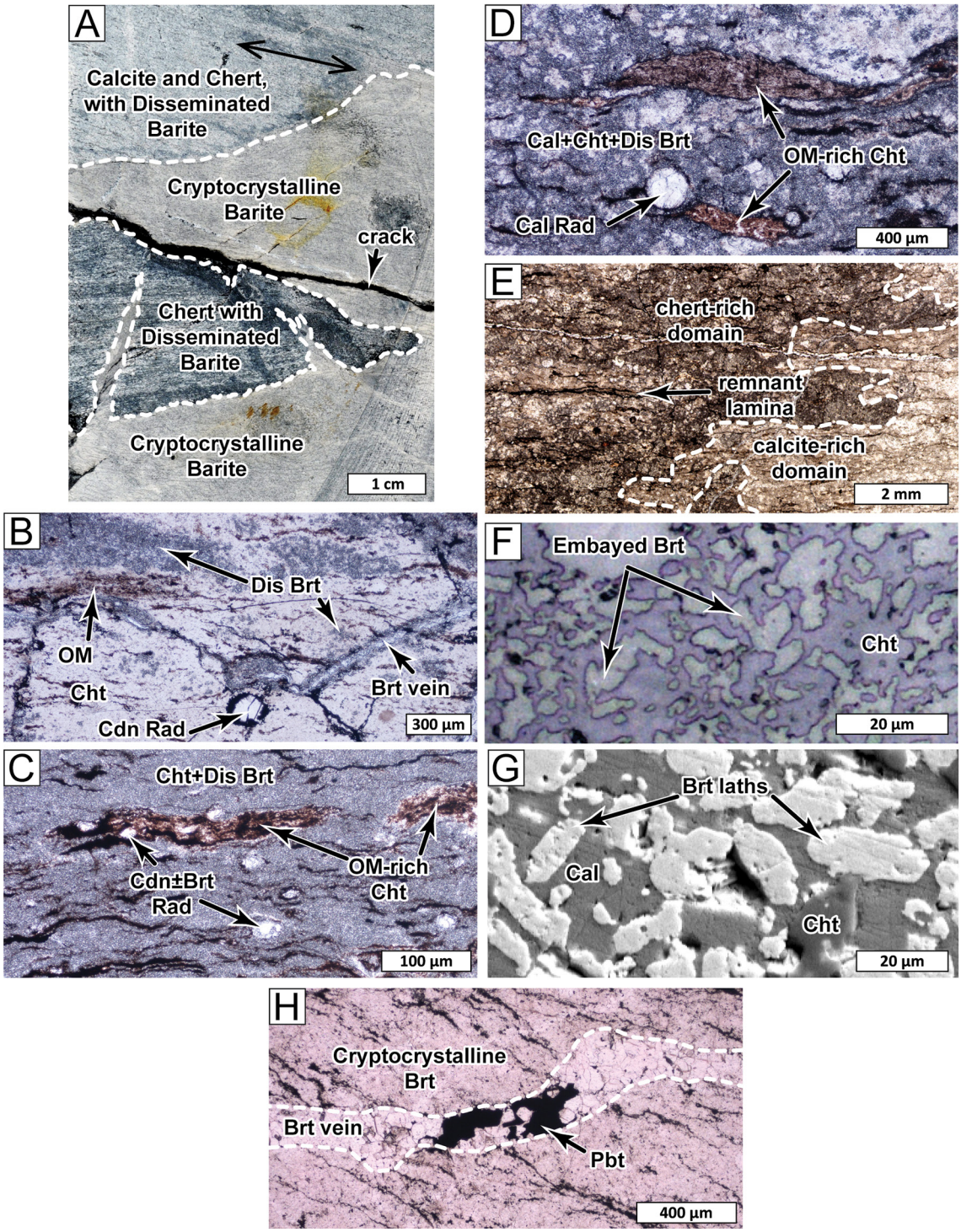

Fig. 7. Massive, laminated barite textures in the Anarraaq barite body. (A) Photograph of core in which massive cryptocrystalline barite crosscuts domains of chert ± calcite with disseminated barite. Black line with arrows indicates orientation of remnant laminae apparent in thin section. (B, C) Plane-polarized light photomicrographs of chert with variable organic content and disseminated barite. In B, barite vein has halo of disseminated barite. (D) Plane-polarized photomicrograph of chert intermixed with calcite; both contain disseminated barite. In B-D, spheres of chalcedony, barite, and calcite form after radiolarians. (E) Plane-polarized photomicrograph of the boundary between chert-rich and calcite-rich baritic domains (dashed line), which is highly irregular and discordant to remnant mudstone laminae. (F) Reflected-light photomicrograph shows disseminated barite in chert has highly irregular to embayed crystal boundaries, suggesting dissolution and remobilization. (G) Backscattered electron image shows disseminated barite laths in calcite, suggesting these crystals were protected from dissolution. (H) Plane-polarized photomicrograph of massive cryptocrystalline barite crosscut by coarsely crystalline barite ± pyrobitumen vein. Samples 809-1913.1 (A, F), 809-1893.2 (B, D, E, H), 809-1852.7 (C). Abbreviations: Brt = barite, Cal = calcite, Cdn = chalcedony, Cht = chert, Dis = disseminated, OM = organic material, Pbt = pyrobitumen, Rad = radiolarian.

Downloaded from http://pubs.geoscienceworld.org/segweb/economicgeology/article-pdf/116/8/1803/5428899/4849_reynolds_et_al.pdf
by Freie Universitaet Berlin user

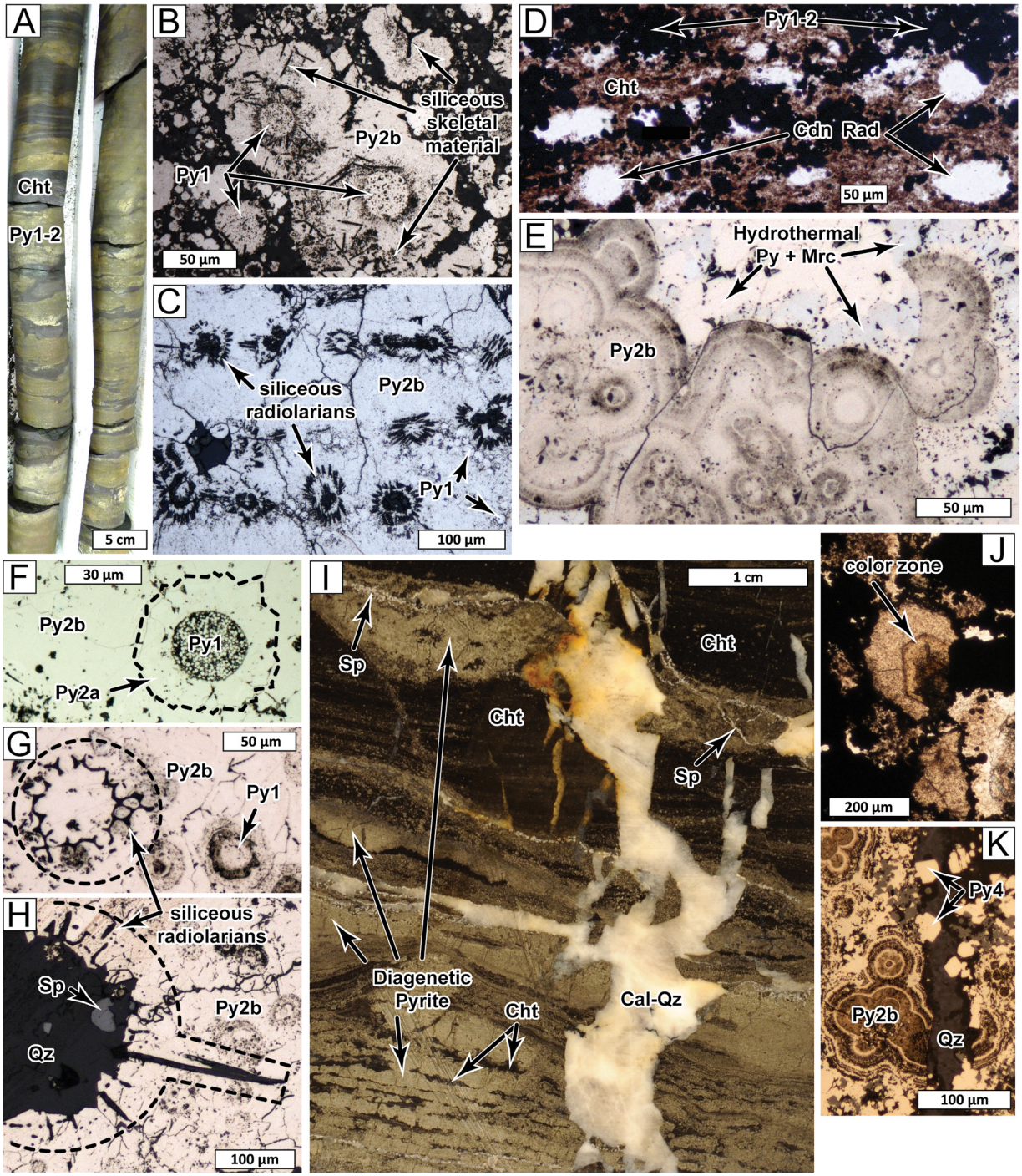

Fig. 8. (A) Photograph of core shows bedded to nodular pyrite that locally underlies massive barite of the barite body. (B, C) Reflected-light photomicrographs from near A show pyrite framboids and spheres enclosed by a later generation of massive fine-crystalline pyrite. Abundant siliceous radiolarians are preserved as fossil hash (B) and layers of intact skeletons (C). (D) Plane-polarized photomicrograph from near A shows chert interbeds contain abundant radiolarians preserved as chalcedony spheres. (E) Reflected-light photomicrograph shows coalescing colloform texture common in diagenetic pyrite of the Upper zone. Reflected-light photomicrographs of diagenetic pyrite in the Lower zone show a pyrite framboid (F) and sphere (G) overgrown by euhedral (F) and massive (F-H) pyrite. Massive pyrite contains siliceous radiolarian skeletal material. (I) Photograph of core showing laminated pyrite in mudstone crosscut by sphalerite veinlets and late calcite-quartz vein. (J) Plane-polarized photomicrograph of sphalerite from I shows crystals contain color zonation despite pale, uniform color in hand specimen. (K) Reflected-light photomicrograph shows cubic pyrite in quartz vein, which crosscuts early Fe sulfide generations. Samples 809 1972-1976ft (A), 809-1980.3 (B), 809-1971.8 (C), 809-1963.7 (D), 1719-2154.8 (E), 923-2404.8 (F), 1713-2352.5A (G, H), 1723-2197.6 (I, J), 923-2204.6 (K). Core photos oriented with up hole toward top of page. Abbreviations: Cal = calcite, Cdn = chalcedony, Cht = chert, Mdst = mudstone, Mrc = marcasite, Py = pyrite, Qz = quartz, Rad = radiolarian, Sp = sphalerite. Numbers indicate paragenetic phases in Figure 9.

Downloaded from http://pubs.geoscienceworld.org/segweb/economicgeology/article-pdf/116/8/1803/5428899/4849_reynolds_et_al.pdf
by Freie Universitaet Berlin user

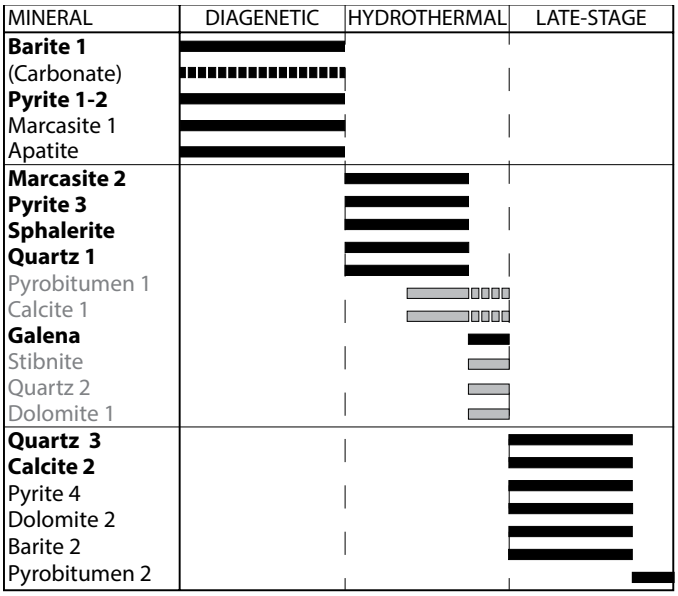

Fig. 9. Paragenesis of the Upper and Lower zones in the Anarraaq sulfide deposit. Carbonate is in parentheses to indicate that its presence is inferred. Grayed minerals observed only in the Lower zone. Bolded minerals are most abundant.

distribution of diagenetic components (Fig. 5B) including an upper interval of mudstone with (pseudomorphs after) barite, a middle interval of very poorly preserved host rock (i.e., of unknown composition) with local intervals or clasts of black mudstone and diagenetic Fe sulfide, and a basal interval of mudstone with abundant diagenetic Fe sulfide layers and nodules. Although the host rock is less well preserved in the southeastern, higher-grade part of the deposit, rare evidence of barite occurs at a similar stratigraphic level in cores 1714 and 923 (Fig. 4B). In the southwest-northeast cross section, intervals of silicified barite in black mudstone occur only in cores 1713 and 1717 (Fig. 6B).

The hydrothermal mineral assemblage of the Lower zone is dominated by marcasite, pyrite, sphalerite, quartz, and galena (Fig. 9). Hydrothermal pyrite and marcasite do not contain biosiliceous inclusions and are coarser and brighter in luster than diagenetic Fe sulfide (Fig. 11F). Some marcasite crystals have been partially replaced by pyrite (Fig. 11F). The Fe sulfide is commonly intermixed with sphalerite at a fine scale, but it also occurs as macroscopic veins, cavity rims (Fig. 11A), vein rims, and rare stalactites (Fig. 11G). Hydrothermal Fe sulfide predates some sphalerite and vice versa, commonly within the same hand sample.

Sphalerite in the Lower zone is highly variable in color (Fig. 11A, B, D), and color zonation within crystals is ubiquitous (Figs. 8J, 10C). Even sphalerite that appears uniform in hand sample shows color zonation in thin section (Fig. 8I, J). Sphalerite occurs disseminated in mudstone (Fig. 11I), as veins (Fig. 11I), as pseudomorphs after barite (Fig. 10C, D), and in complex mineralized breccias (Fig. 11A, B). Sphalerite veins crosscut mudstone and diagenetic Fe sulfide and barite (Figs. 10A, 11I). Veins are locally associated with disseminated sphalerite in mudstone, which may be abundant enough to obscure the host lithology (Fig. 11I; dashed circles). Sphalerite preferentially replaces barite rather than the surrounding mudstone (Fig. 10A). Zoned, euhedral sphalerite crystal outlines suggest that barite was entirely dissolved before sphalerite grew in the resulting cavities (Fig. 10C).

The higher-grade parts of the deposit are characterized by mineralized breccias that contain a complex mixture of sulfides, quartz, calcite, mudstone, and diagenetic Fe sulfide (Fig. 11A, B). In some places, mineralized breccias are stratiform between undisturbed layers of mudstone and diagenetic Fe sulfides (Fig. 11H). Breccias contain irregular cavities up to 10 cm across that are lined with hydrothermal Fe sulfide (Fig. 11A), euhedral calcite (Fig. 11J), or sphalerite (Fig. 11D). Cavities contain internal sediment predominantly composed of sphalerite and quartz (Fig. 11A, D). Sphalerite forms snow-on-roof textures (Fig. 11D) and is intergrown with quartz (Fig. 11C). Quartz is euhedral or microcrystalline and contains organic matter including rounded pyrobitumen bodies inferred to have formed from hydrocarbon bubbles trapped at the time of hydrothermal mineralization (Fig. 11C). Internal sediment with minor sphalerite and abundant quartz is very dark gray and can easily be mistaken for Ikalukrok mudstone (Fig. 11J). Multiple cavities over several meters of core contain identical internal stratigraphic sequences, suggesting interconnection at the time of internal sedimentation and confirming lithification occurred before the main stage of hydrothermal mineralization.

Galena mainly occurs in the zones of higher-grade Zn mineralization. In some places, galena and sphalerite appear to be coeval at the hand sample scale (Fig. 11D) but thin sections reveal that galena clearly crosscuts sphalerite (Fig. 11E) and hydrothermal Fe sulfides. Locally, galena contains rare stibnite or is intergrown with rhombic dolomite crystals (Fig. 11E) or anhedral, inclusion-rich quartz.

In the Lower zone, the hydrothermal mineralization decreases in intensity from southeast to northwest (Figs. 5C, 6C); in the southeast, hydrothermal sulfides completely replace the host rock, whereas in the northwest, significant amounts of host rock are preserved. Common textures in the southeast include multiple generations of sphalerite, abundant ruby-red and brown sphalerite, abundant galena, mineralized breccias, and cavities with internal sediment. In the northwest, the uppermost part of the Lower zone is characterized by hydrothermal veining and preferential replacement of barite over surrounding mudstone, the middle to upper part shows intervals of near-complete host-rock replacement, and the base is characterized by relatively minor sphalerite and Fe sulfide (Fig. 10I).

Late-stage quartz and calcite occur in the center of veins (Fig. 10A) and at the stratigraphic top of some cavities rimmed with hydrothermal sulfides and generally crosscut all earlier minerals (Figs. 8I, 11H). Rare local dolomite and barite also occur with late calcite. Pyrobitumen locally cements space between calcite crystals. Cubic pyrite commonly occurs at the edges of calcite and quartz veins that crosscut earlier generations of Fe sulfide (Fig. 8K). Late-stage minerals may represent a final episode of Mississippian hydrothermal mineralization, Brookian (Mesozoic) tectonism, or both.

Sulfide deposit—Upper zone: The Upper zone is like the Lower zone in many ways (Fig. 9); only major differences are highlighted here. Quartz ± disseminated sphalerite pseudomorphs after barite laths are relatively rare and occur in the

Downloaded from http://pubs.geoscienceworld.org/segweb/economicgeology/article-pdf/116/8/1803/5428899/4849_reynolds_et_al.pdf
by Freie Universitaet Berlin user

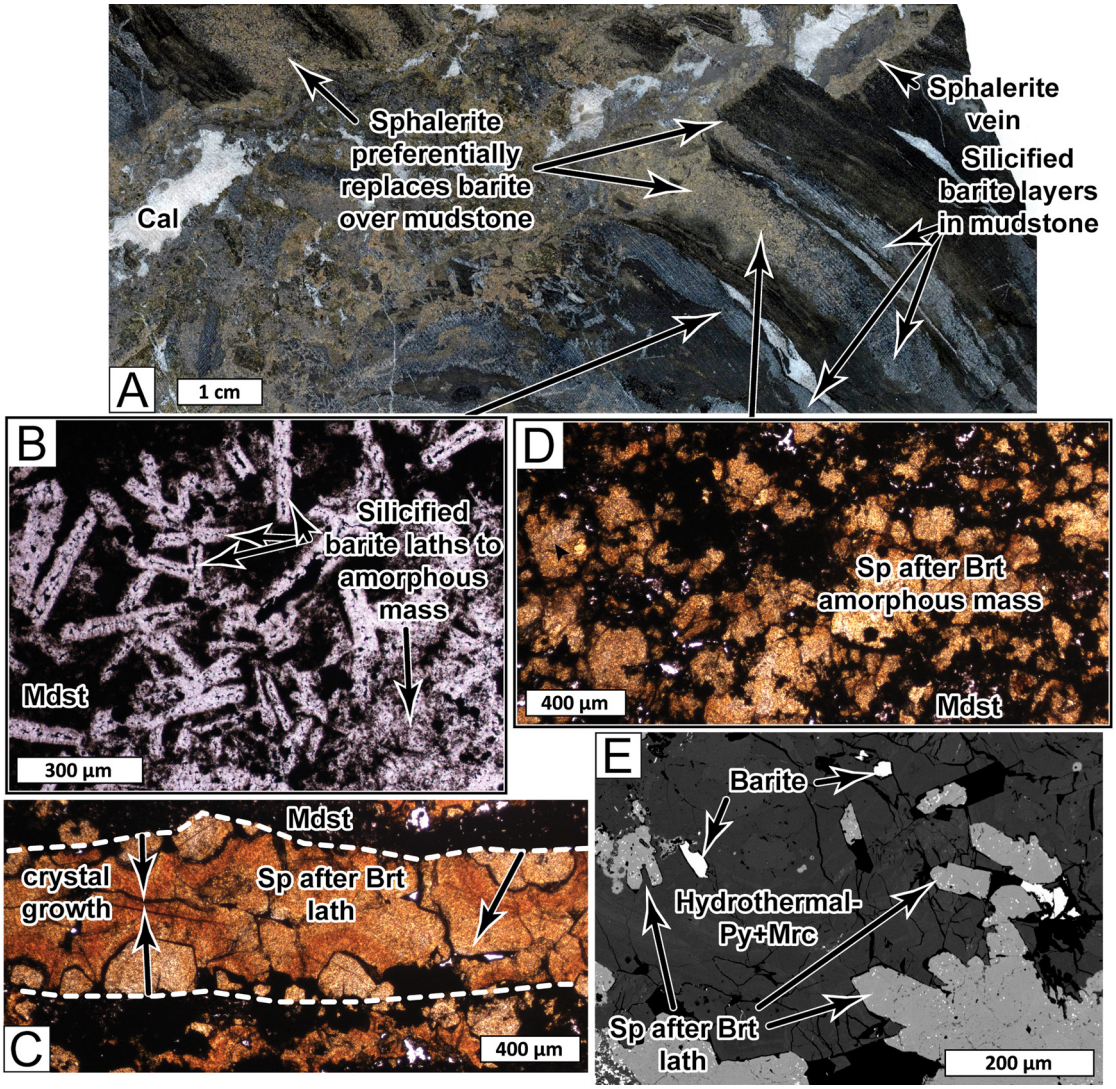

Fig. 10. Lower zone barite of the Anarraaq sulfide deposit. (A) Photograph of drill core with up hole toward right of page. Sphalerite vein crosscuts interbedded mudstone and silicified barite. Sphalerite preferentially replaces barite rather than the surrounding mudstone. Plane-polarized light photomicrographs show (B) silicified barite textures range from distinctive laths to amorphous masses. (C) Sphalerite pseudomorph after barite lath is composed of zoned crystals that indicate nucleation at the edge of the former barite crystal and inward growth into open space, suggesting barite was completely dissolved prior to sphalerite precipitation. (D) Distinctive lath textures are absent in some sphalerite after barite. (E) Backscattered electron image of barite and sphalerite pseudomorphs after barite laths. Samples 1717-2317 (A-D) and 923-2251.2 (E). Abbreviations: Brt = barite, Cal = calcite, Mdst = mudstone, Mrc = marcasite, Py = pyrite, Sp = sphalerite.

upper half of the zone (Figs. 5B, 6B). Diagenetic Fe sulfide nodules are generally smaller in diameter (<1 cm; Fig. 12A) than those in the Lower zone. On a microscopic scale, diagenetic Fe sulfide overgrowths may consist of coalescing colloform features (Fig. 8E) but also contain abundant siliceous microfossil fragments, as in the Lower zone. Most of the Upper zone is characterized by abundant sphalerite with local preservation of black mudstone and diagenetic pyrite. The basal part of the zone is dominantly mudstone with abundant Fe sulfide layers and nodules. Rarely, layers of tightly packed framboidal, spheroidal, or euhedral pyrite occur at both the top and bottom of the main zone of Zn-Pb mineralization (Figs. 5B, 6B).

Sphalerite in the Upper zone is distinctive in that it displays only subtle color variations in hand sample (cream, pale tan, pale pink; Fig. 12C) that are controlled by the relative concentrations of sphalerite, quartz, and mudstone (Fig. 12D-F). No color zonation is displayed within sphalerite crystals (Fig. 12F). In most places, very fine sphalerite is disseminated in microcrystalline quartz, but rare euhedral quartz crystals contain sphalerite inclusions (Fig. 12E, G) and are enclosed by massive sphalerite (Fig. 12E). Although these textures are like the internal sediment of the Lower zone, no well-defined cavities are observed in the Upper zone. Sphalerite also occurs as laminae in mudstone (Fig. 12A), typically in the basal part of the zone (Fig. 5C). Hydrothermal pyrite and marcasite overlap sphalerite precipitation and have a range of textures similar to that in the Lower zone but are generally finer grained; no stalactites have been observed. Galena

Downloaded from http://pubs.geoscienceworld.org/segweb/economicgeology/article-pdf/116/8/1803/5428899/4849_reynolds_et_al.pdf
by Freie Universitaet Berlin user

postdates sphalerite but also forms subhedral crystals up to several millimeters across in mudstone (Fig. 12H). Overall, veins of hydrothermal minerals are much less common relative to the Lower zone. The Upper zone is smaller and less laterally extensive and there is no lateral trend in intensity of base metal mineralization, although the thickest interval of high-grade Zn-Pb mineralization is in the southwesternmost drill core 809 (Fig. 6C).

Rhenium-osmium geochronology

Results from Re-Os analyses of mudstone and pyrite samples are reported in Table 1. The mudstone contains the highest concentrations of Re and Os (19.4–40.5 ppb and 888–1,709 ppt, respectively), and diagenetic pyrite has the lowest concentrations (0.47–1.30 ppb and 16.57–29.35 ppt). Hydrothermal pyrite contains intermediate values of Re (2.86–4.80 ppb) and Os (22.30–28.96 ppt). The hydrothermal pyrite is the most radiogenic with $^{187}Os/^{188}Os$ of 6.79–12.00; mudstone and diagenetic pyrite samples are characterized by $^{187}Os/^{188}Os$ of less than 2.

Regression of seven mudstone analyses yields an age of 339.1 ± 8.3 Ma (mean square of weighted deviates [MSWD] = 19) with an initial Os ratio of 0.375 ± 0.019 (Fig. 13A). Analyses of six diagenetic pyrites yield an isochron with an age of 333.0 ± 7.4 Ma (MSWD = 1.08) and an initial Os ratio of 0.432 ± 0.025 (Fig. 13A). Results from three hydrothermal pyrite analyses are reported, and although these are not sufficient to build a meaningful isochron, the data points lie very close to the diagenetic pyrite isochron. Regression of all pyrite analyses together yields an age of 334.4 ± 5.3 Ma (MSWD = 3.7) and initial Os ratio of 0.422 ± 0.081 (Fig. 13B), similar, within the resolution of the analytical results, to the diagenetic-only regression. Furthermore, all pyrite analyses from this study lie very close to the isochron reported by Morelli et al. (2004) for hydrothermal pyrite from the Main deposit. When the analyses from both studies are regressed together, they yield an age of 336.0 ± 3.9 Ma (MSWD = 29) with an initial Os ratio of 0.34 ± 0.11 (Fig. 13C), which is within the uncertainty of the results of Morelli et al. (2004; 338.3 ± 5.8 Ma, initial Os of 0.20 ± 0.21) and of this study.

Discussion

Diagenetic and hydrothermal processes

Anarraaq barite body: The Anarraaq barite body formed when diagenetic fluid bearing methane and barium vented into sulfate-bearing pore water or marine bottom waters (Johnson et al., 2004, 2009). In agreement with the previous studies (Johnson et al., 2004; Kelley et al., 2004b), there is abundant textural evidence that barite precipitated below the sediment surface, including sedimentary fabrics that are crosscut by barite (Fig. 7A) and veins that are interpreted to be feeders for disseminated barite (Fig. 7B). The location of the SMT and associated diagenetic barite precipitation relative to the seafloor is primarily controlled by the upward flux of methane, the seawater sulfate concentration, and the rate of sedimentation (Jørgensen et al., 2004; Arning et al., 2015). If the SMT advances upward toward preexisting diagenetic baritic strata, barite may undergo dissolution and reprecipitation (Snyder et al., 2007).

Kelley at al. (2004b) interpreted the calcareous components of the Anarraaq barite body to be mass flow deposits overprinted by methane-transported diagenetic barite; however, here for the first time we present petrographic data that indicate that at least some of calcite in the barite body is authigenic: it crosscuts sedimentary laminae (Fig. 7E) and postdates some barite generations (Fig. 7G). In the massive, laminated part of the barite body, well-formed barite crystals only occur enclosed in calcite, suggesting that early formation of authigenic calcite preserved some barite from dissolution. The morphology of these crystals is similar to that of samples collected from modern methane seeps in the northern Gulf of Mexico (Feng and Roberts, 2011).

The abundance and clustered nature of framboids in the nodular to layered pyrite that locally underlies the Anarraaq barite body (Fig. 8C) are characteristic of framboids formed at modern SMTs (Lin, Q., et al., 2016). The pyrite overgrowths are certainly secondary and are similar to overgrowths reported in modern SMT sediment (Lin, Q., et al., 2016; Lin, Z., et al., 2016) and the preservation of abundant siliceous radiolarian skeletons suggests pyrite formed relatively early during burial.

Fig. 11. Mineralized textures from the Lower zone of the Anarraaq sulfide deposit. (A) Photograph of core containing mineralized breccia and cavity (dashed black line) rimmed in Fe sulfide and filled with internal sediment. Dashed white line marks bedding surface between layers of cryptocrystalline and euhedral quartz internal sediment. (B) Plane-polarized light photomicrograph of mineralized breccia in A, which contains clasts of mudstone and sphalerite enclosed in a complex mixture of quartz, sphalerite, and organic material. (C) Plane-polarized light photomicrograph of internal sediment in A. Dashed line marks bedding surface between cryptocrystalline and euhedral quartz, both of which are intergrown with sphalerite. Note subrounded pyrobitumen occurrence, which is interpreted to have been a hydrocarbon bubble trapped at the time of hydrothermal mineralization. (D) Photograph of core shows cavity rimmed in sphalerite, galena, and local Fe sulfide and filled with internal sediment primarily composed of quartz and sphalerite. Note snow-on-roof sphalerite textures. (E) Reflected-light photomicrograph shows galena crosscuts sphalerite leaving highly irregularly shaped sphalerite islands in galena. Euhedral dolomite is intergrown with galena. (F) Reflected-light photomicrograph shows hydrothermal euhedral marcasite crystal partially replaced by pyrite (dashed line marks boundary). Note the overall complexity of pyrite and marcasite textures. (G) Photograph of core shows Fe sulfide stalactites enclosed in calcite. (H) Photograph of core shows undisturbed layers of mudstone and diagenetic Fe sulfides overlying stratiform mineralized breccia. (I) Photograph of core shows Ikalukrok mudstone, which contains diagenetic Fe sulfide, sphalerite-galena veins, and disseminated sphalerite. Disseminated sphalerite locally obscures host lithology (dashed-line circle). (J) Photograph of core shows euhedral calcite crystals enclosed by internal sediment with subtle laminated texture (parallel to dashed line). In this sample, internal sediment is very dark gray because it is composed of quartz >> sphalerite and could easily be mistaken for Ikalukrok mudstone. Samples 1713-2495 (A-C), 1714-2471.2 (D), 923-2385.3 (E), 923-2376.6 (F), 1716-2303.5 (G), 1716-2347 (H), 1713-2536 (I), 1716-2344.4 (J). All core photos are oriented with up hole toward top of page. Abbreviations: Cal = calcite, Dol = dolomite, Gn = galena, IS = internal sediment, Mdst = mudstone, Mrc = marcasite, OM = organic material, Pbt = pyrobitumen, Py = pyrite, Qz = quartz, Sp = sphalerite.

Downloaded from http://pubs.geoscienceworld.org/segweb/economicgeology/article-pdf/116/8/1803/5428899/4849_reynolds_et_al.pdf
by Freie Universitaet Berlin user

The bisulfide (HS^-) produced by SD-AOM at the SMT produces pyrite when it reacts with dissolved iron. Some dissolved iron originates within SMT sediment, but excess HS^- can also accumulate and diffuse beyond the SMT. Stratiform pyrite has been observed to form below the SMT where excess HS^- encounters upward-diffusing Fe^{2+} sourced from deeper sediment (Jørgensen et al., 2004). Thus, we interpret the pyrite (Py1, Py2) to form from methane-driven diagenetic processes.

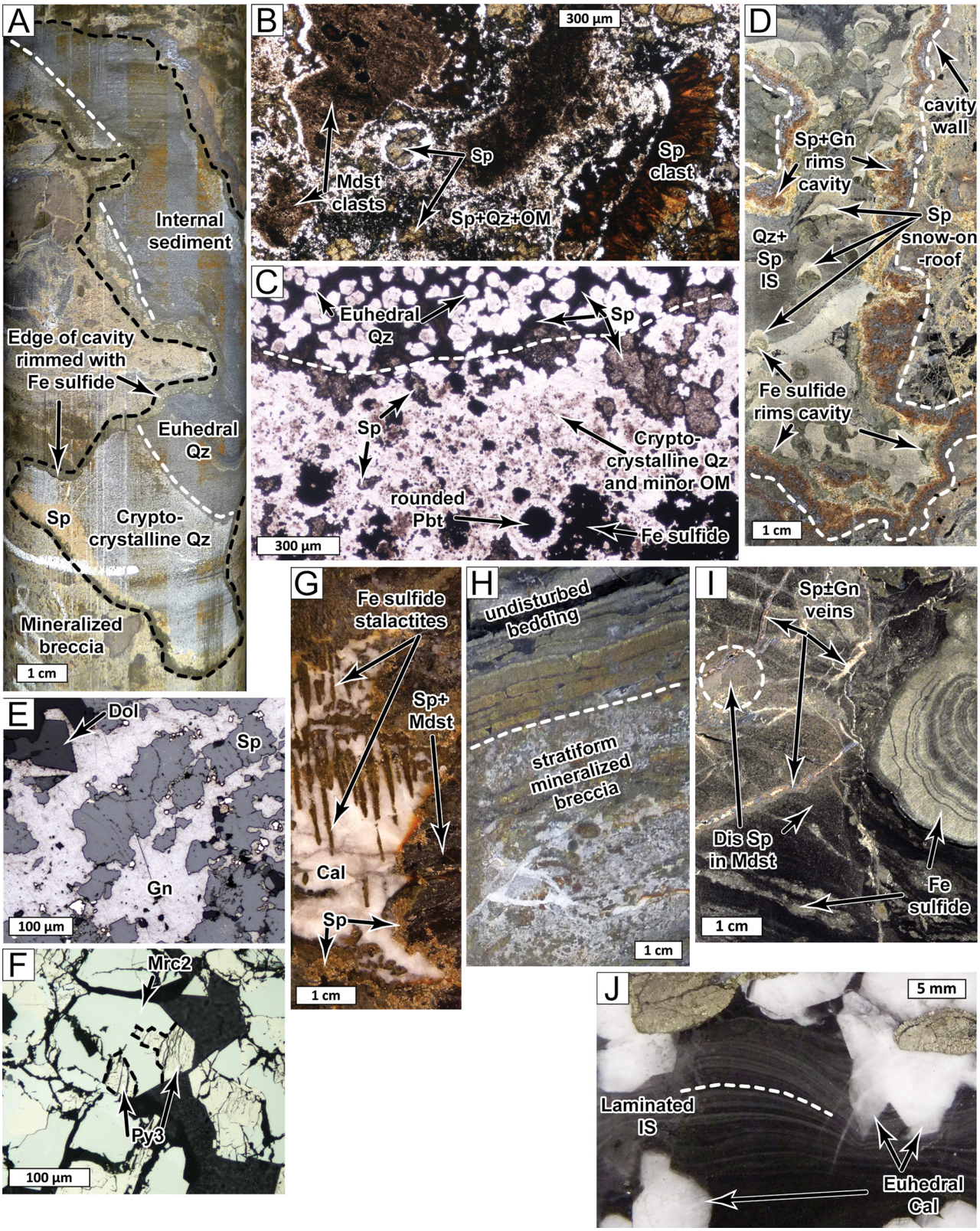

Downloaded from http://pubs.geoscienceworld.org/segweb/economicgeology/article-pdf/116/8/1803/5428899/4849_reynolds_et_al.pdf
by Freie Universitaet Berlin user

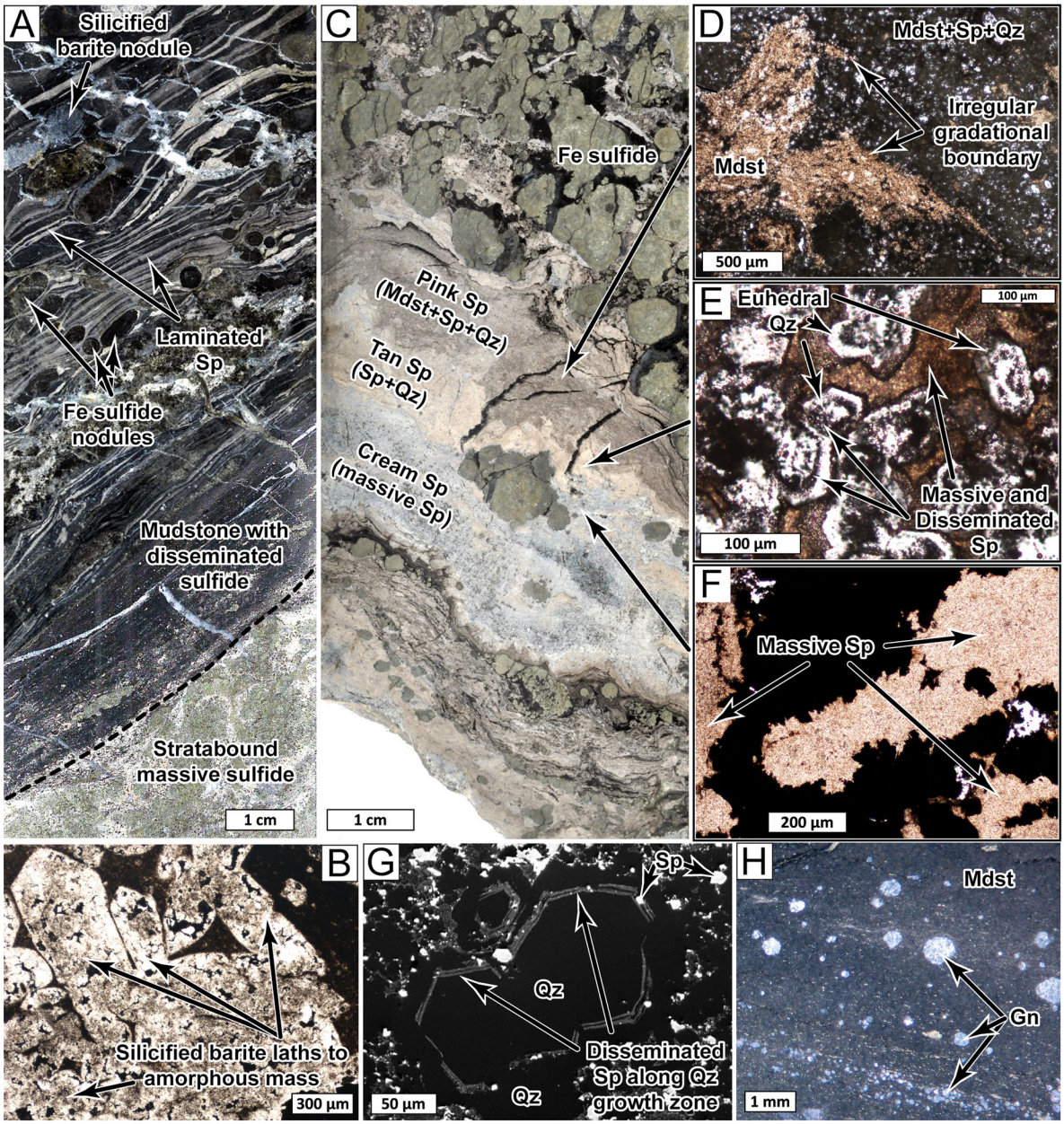

Fig. 12. Mineralized textures from the Upper zone of the Anarraaq sulfide deposit. (A) Photograph of core showing laminated sphalerite in Ikalukrok mudstone with diagenetic Fe sulfide and silicified barite nodules. Note sharp transition to stratabound massive sulfide at bottom of sample. (B) Plane-polarized light photomicrograph of silicified barite in A shows textures ranging from laths to amorphous mass. Elsewhere in the sample, pseudomorphs after barite also contain disseminated sphalerite and Fe sulfide. (C) Photograph of core shows subtle variations in sphalerite color. Plane-polarized light photomicrographs from the same sample show (D) pink domains contain a mixture of mudstone, quartz, and sphalerite. The boundaries between mudstone and quartz-sphalerite are irregular and somewhat gradational. (E) Tan domains contain a mix of quartz and sphalerite. This sample displays rare euhedral quartz crystals with sphalerite inclusions, enclosed by massive sphalerite. (F) Cream-colored domains contain massive sphalerite with no color zonation. (G) Backscattered electron image shows disseminated sphalerite along a growth zone in euhedral quartz. (H) Photograph of core showing galena crystals in mudstone. Samples 1719-2154 (A, B), 809-2332.7 (C-F), 923-2202.3 (G), 809-2396.7 (H). Core photos oriented with up hole toward top of page. Abbreviations: Gn = galena, Mdst = mudstone, Qz = quartz, Sp = sphalerite.

The deposit-scale stratigraphic relationship between barite, authigenic carbonate, and diagenetic pyrite in the Anarraaq barite body is consistent with what is expected in SMT zones (e.g., Lash, 2015; Fig. 4), and diagenetic calcite after barite is reported in some locations (e.g., Dean and Schreiber, 1978). However, the thickness of the Anarraaq barite body (~50–100 m) is much greater than intervals of barite enrichment reported in modern SMT zones (from <1 cm to 3 m; e.g., Brumsack, 1986; Torres et al., 1996; Snyder et al., 2007) or even the thickest reported modern methane seep barite deposits (~10 m at Sea of Okhotsk and at the California Borderlands; Greinert et al., 2002; Gwiazda et al., 2019). The

Downloaded from http://pubs.geoscienceworld.org/segweb/economicgeology/article-pdf/116/8/1803/5428899/4849_reynolds_et_al.pdf
by Freie Universitaet Berlin user

Table 1. Re-Os Isotope Results for Anarraaq

Sample name	Sample type	Re (ppb)	Os (ppt)	$^{187}Re/^{188}Os$	±2σ	$^{187}Os/^{188}Os$	±2σ	Rho
923-2123-A1	Shale	23.1	1,253	97.98	0.3	0.925	0.002	0.4
923-2123-A2	Shale	24.4	1,126	116.90	0.4	1.046	0.003	0.4
923-2123-B-2	Shale	21.8	888	133.99	0.5	1.135	0.003	0.4
923-2123-D-2	Shale	24.1	1,218	105.93	0.4	0.970	0.002	0.3
923-2123-G-2	Shale	19.4	1,025	100.69	0.4	0.944	0.002	0.4
923-2123-M	Shale	34.9	1,709	109.48	0.4	1.001	0.002	0.3
923-2123-N	Shale	40.5	1,021	229.63	0.8	1.675	0.004	0.4
1716-2520.8 A	Pyrite-diagenetic (Py1-2)	1.30	28.98	265.42	1.52	1.91	0.01	0.54
1716-2520.8 Y	Pyrite-diagenetic (Py1-2)	0.47	19.21	135.51	1.99	1.20	0.03	0.52
1716-2520.8 C+3	Pyrite-diagenetic (Py1-2)	0.80	23.51	192.63	1.31	1.51	0.01	0.44
1716-2520.8 C+4	Pyrite-diagenetic (Py1-2)	0.61	29.35	112.60	1.91	1.06	0.03	0.54
1716-2520.8 D+2	Pyrite-diagenetic (Py1-2)	0.85	28.89	165.15	3.11	1.34	0.04	0.60
1716-2520.8 X	Pyrite-diagenetic (Py1-2)	0.52	16.57	175.60	1.48	1.40	0.01	0.49
1723-2104.5 A-3	Pyrite-hydrothermal (Py3)	4.80	28.96	2,034.22	17.84	12.00	0.16	0.58
1723-2104.5 D+2	Pyrite-hydrothermal (Py3)	4.36	26.63	1,901.08	12.76	10.94	0.08	0.82
1723-2104.5 D+3	Pyrite-hydrothermal (Py3)	2.86	22.30	1,153.74	9.03	6.79	0.08	0.58

Anarraaq barite body also lacks the macrofauna and towers typically associated with seep deposits or any truly laminated textures that indicate deposition on the seafloor (Johnson et al., 2004; this study). The rock record contains other thick barite beds that appear to be diagenetic. For example, the Late Devonian barite occurrences found in the Selwyn basin, Canada, are 100–150 m thick and have isotopic (S, Sr) compositions that suggest they formed in a diagenetic environment (Fernandes et al., 2017). At times of steady-state diagenesis, the formation of barite units requires either high methane

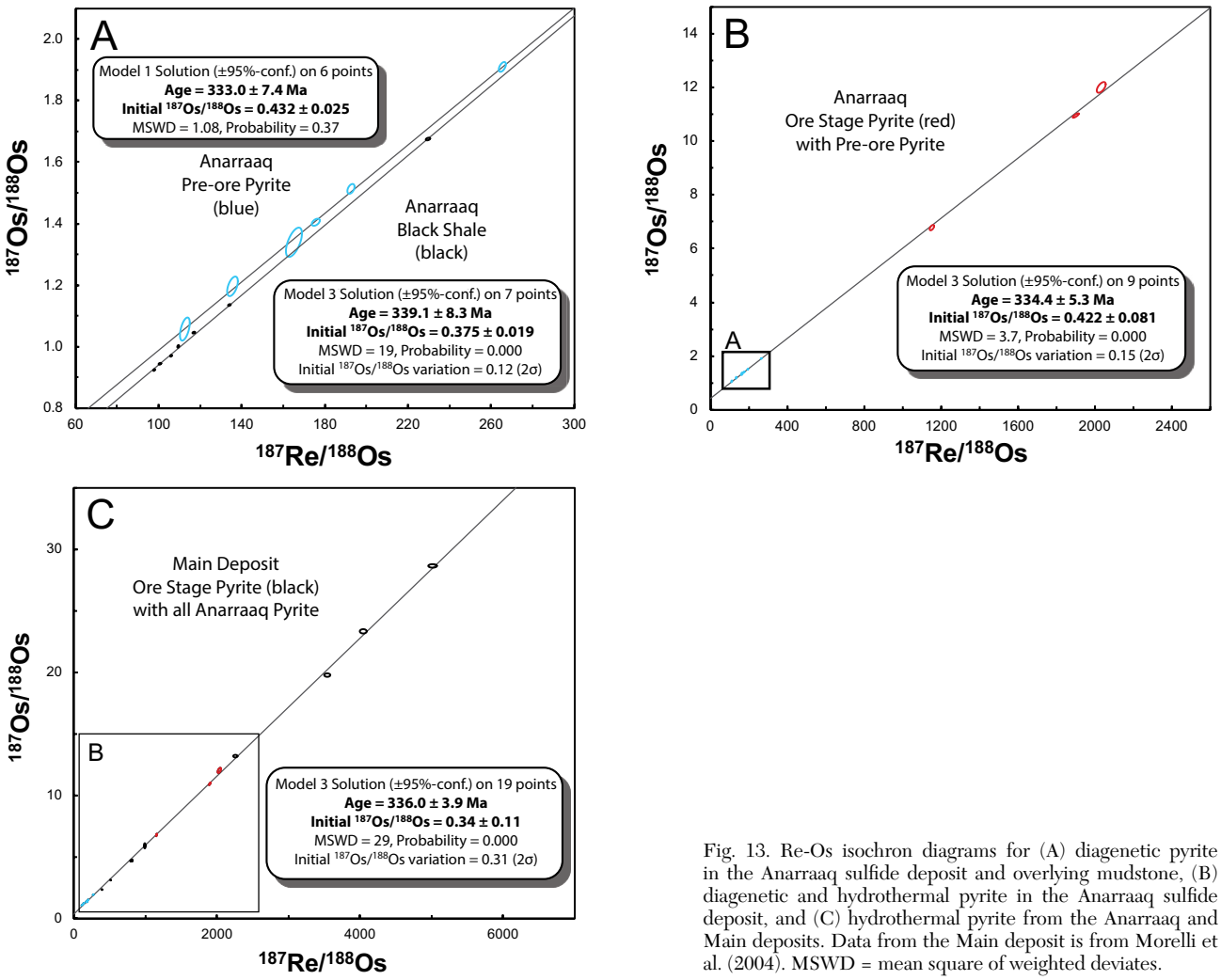

Fig. 13. Re-Os isochron diagrams for (A) diagenetic pyrite in the Anarraaq sulfide deposit and overlying mudstone, (B) diagenetic and hydrothermal pyrite in the Anarraaq sulfide deposit, and (C) hydrothermal pyrite from the Anarraaq and Main deposits. Data from the Main deposit is from Morelli et al. (2004). MSWD = mean square of weighted deviates.

Downloaded from http://pubs.geoscienceworld.org/segweb/economicgeology/article-pdf/116/8/1803/5428899/4849_reynolds_et_al.pdf
by Freie Universitaet Berlin user

fluxes (and/or sulphate fluxes) or lower fluxes over long time periods (see Johnson et al., 2004, who calculate 50,000 y to form 50 m of barite). However, upwelling environments on continental margins are areas of nonsteady-state diagenetic processes, in which key variables (sedimentation rate, organic matter deposition, methane flux) vary on timescales from days to thousands of years (Kasten et al., 2003). Changes in the sedimentation rates can change the depth of the SMT and allow for recycling and reprecipitation of authigenic minerals; these processes are not well quantified in modern systems except in a few examples (Wehrmann et al., 2013) but nonsteady-state diagenetic processes may allow for thicker beds of authigenic minerals to be formed over longer time periods. In addition, to maximize these processes, the host sediment must be highly permeable. Both the Selwyn basin and Kuna basin barite units are hosted in radiolarian-rich, biosiliceous sediments; radiolarite can maintain porosities of up to 70% at 500 m (Isaacs, 1982). This may have allowed for the accumulation of abundant diagenetic components even in the subsurface (Magnall et al., 2015, 2020a).

Anarraaq sulfide deposit: The diagenetic components of the host rock in the Anarraaq sulfide deposit have striking compositional, textural, and stratigraphic similarities to the Anarraaq barite body. Barite and layered to nodular pyrite occur in both the Upper zone and Lower zone, and diagenetic Fe sulfide textures include framboids and overgrowths with well-preserved radiolarian skeletal material. We suggest, therefore, that the sulfide zones overprinted preexisting SMTs in the subsurface, similar to the one preserved in the barite body. This contrasts previous interpretations that layered to nodular pyrite associated with Zn-Pb mineralization in the Red Dog district is hydrothermal (Kelley et al., 2004b; Blevings et al., 2013).

The poorly preserved intervals of host rock indicate that a large amount of material underwent extensive dissolution during hydrothermal mineralization. Almost all the diagenetic barite in the Anarraaq sulfide deposit was replaced by quartz and sulfide minerals (Figs. 10, 12A, B). In the Lower zone, the colloform sphalerite pseudomorphs after barite indicate open-space growth (e.g., Fig. 10C), and we interpret the barite crystals to have been completely dissolved prior to sphalerite precipitation. For this to be possible, the mudstone surrounding the barite crystal must have been well lithified to prevent collapse into the open space of the dissolved crystal. The presence of large, mineralized cavities (Fig. 11A, D) and stratabound mineralized breccias (Fig. 11H) also suggests a fully cemented host rock. It seems that barite dissolution alone is unlikely to explain the large cavities found in the Lower zone. Of the original constituents of the host rock, the dissolution of siliceous mudstone or pyrite to form cavities up to 10 cm across seems relatively unlikely, although we would expect the solubility of a biosiliceous (opaline) mudstone to be somewhat higher than a clastic (quartz- and clay-rich) mudstone. Abundant phosphorite beds have been reported in other parts of the Kuna Formation (Dumoulin et al., 2014), but only minor local apatite nodules have been observed in the Ikalukrok unit in the Red Dog district (Slack et al., 2004). Therefore, we agree with Kelley et al. (2004b) that carbonate is the most likely precursor to the cavities. Whereas Kelley et al. (2004b) concluded that this carbonate was sedimentary in origin, we suggest that dissolution of authigenic carbonate that formed in association with diagenetic barite may have also contributed to the porosity and permeability exploited by the hydrothermal system.

The Upper zone contains euhedral quartz enclosed in sphalerite (Fig. 12E) that is texturally similar to internal sediment filling cavities of the Lower zone (Fig. 11C) but lacks clearly defined cavity boundaries (Fig. 12C). In combination with the presence of irregular and gradational boundaries between mudstone and quartz-sphalerite domains (Fig. 12C, D) and the relative rarity of veining and angular mudstone clasts in the Upper zone, this suggests that Upper zone sediment may have been less completely cemented than the Lower zone at the time of Zn-Pb mineralization.

Original stratigraphic relationship of the Anarraaq barite body and sulfide deposit

The displacements on the thrust faults at Anarraaq are poorly constrained. If the displacements were small in magnitude, the present-day configuration of the Lower zone, Upper zone, and barite body could reflect stratigraphic relationships close to the original. If the displacements were more significant, the two zones of Zn-Pb mineralization and the barite body may have formed lateral to each other and were subsequently structurally superimposed. Low-angle faults appear to cut both up and down section in the inferred direction of transport (Fig. 6), indicating that Brookian deformation was more complex than the simple stacking of thrust imbricates in a duplex system, as suggested by De Vera et al. (2004). Several explanations are possible. First, the lenticular nature of the Upper and Lower zones may reflect large variations in strata thickness due to differential compaction, causing thrust faults to locally cut down section. Second, the direction of tectonic transport may not have been parallel to the cross section shown in Figure 6, and the ramps shown in the section may therefore be lateral or oblique ramps, rather than frontal ramps as implied by the vergence shown by Blevings et al. (2013). Third, thrusts may have been emplaced out of sequence during Brookian deformation, possibly because of the laterally heterogeneous mechanical properties of the massive sulfide bodies. More work is required to resolve this issue.

Baritic strata of the Lower zone correlate well among cores 1723, 1716, 1712, 1717, and 1713, with a trend of gradual thickening toward the most intensely mineralized part of the deposit (Figs. 5B, 6B). In contrast to this trend, cores 1714 and 808 show a thinning or absence of barite and a dramatic thinning in the overall thickness of the Lower zone (Fig. 6B). This may reflect the original geometry of the diagenetic barite or later structural modification. Although the main thickness of the Upper zone is in the northwestern part of the sulfide deposit, intervals of Upper zone-style mineralization farther northeast are characterized by pervasive shearing that clearly postdates mineralization. This geometry could be partly inherited from a heterogeneous original distribution of mineralized units; however, the evidence for deformation strongly suggests that fragments of Upper zone material were transported along a fault.

Re-Os constraints on the age and Os sources for Anarraaq

The Re-Os isochron ages for the black mudstone just above the Anarraaq sulfide deposit (339.1 ± 8.3 Ma) and the diage-

Downloaded from http://pubs.geoscienceworld.org/segweb/economicgeology/article-pdf/116/8/1803/5428899/4849_reynolds_et_al.pdf
by Freie Universitaet Berlin user

netic pyrite from within the Anarraaq sulfide deposit (333.0 ± 7.4 Ma) are within error of the Re-Os isochron age of hydrothermal pyrite in the Main deposit in the mine area (338.3 ± 5.8 Ma; Morelli et al., 2004). Although the three data points for hydrothermal pyrite at Anarraaq are not sufficient to create a meaningful isochron, the fact that they plot very close to the diagenetic pyrite isochron suggests that the Re-Os systematics of hydrothermal pyrite are not grossly different from those of diagenetic pyrite. Overall, the data are consistent with contemporaneous Zn-Pb mineralization at Anarraaq and the Main deposit.

Although the contact between the Anarraaq sulfide deposit and the overlying nonmineralized sediment is a thrust fault, the overlapping Re-Os isotope ages are compatible with the idea that sediment deposition and hydrothermal mineralization were relatively close in age. As in the Main deposit in the mine area, the textural evidence at Anarraaq indicates that Zn-Pb mineralization was replacive, but the absolute timescale of replacement cannot be resolved with the current Re-Os isochron ages.

Initial Os composition

The global marine Os record is not well constrained during the Carboniferous, but there are several published Re-Os isochrons for Late Devonian mudstones in western Canada and one for a Lower-Middle Pennsylvanian mudstone in the eastern United States (Fig. 14). These data indicate that marine $^{187}Os/^{188}Os$ was between 0.37 and 0.64 in the Late Devonian (~360 Ma; Creaser et al., 2002; Selby and Creaser, 2003, 2005) and no higher than 0.72 in the Lower to Middle Pennsylvanian (323 ± 7.8 Ma; Geboy et al., 2015). The initial $^{187}Os/^{188}Os$ value for the Anarraaq mudstone isochron (0.375 ± 0.019) is broadly consistent with these data and may be representative of global marine Os composition.

Slack et al. (2015) proposed that Middle Mississippian (~335 Ma) marine $^{187}Os/^{188}Os$ was much higher (~1.08) and that Ikalukrok mudstones with lower initial $^{187}Os/^{188}Os$ record the local/intermittent influence of a metalliferous hydrothermal fluid venting into the seawater. This interpretation is based on single sample analyses and calculated initial $^{187}Os/^{188}Os$ values rather than full isochrons, which makes it difficult to assess the effects of possible postdepositional disturbance of the Re-Os system. To increase the global marine $^{187}Os/^{188}Os$ composition from 0.64 in the Late Devonian to 1.08 in the Middle Mississippian would require a large increase in radiogenic Os input via continental weathering—that is, an increase on par with what has been observed in more recent geologic history during the rise of the Himalayan mountains (Turekian and Pegram, 1997; Peucker-Ehrenbrink and Ravizza, 2000). The marine $^{87}Sr/^{86}Sr$ ratio is a proxy for global rates of continental weathering and is relatively well constrained over Earth history (Burke et al., 1982; Veizer et al., 1999). Mississippian marine $^{87}Sr/^{86}Sr$ was equal to, or lower than, Late Devonian values (Denison et al., 1994). It therefore seems unlikely that Mississippian global marine $^{187}Os/^{188}Os$ would have been significantly higher than Late Devonian values, although we can-

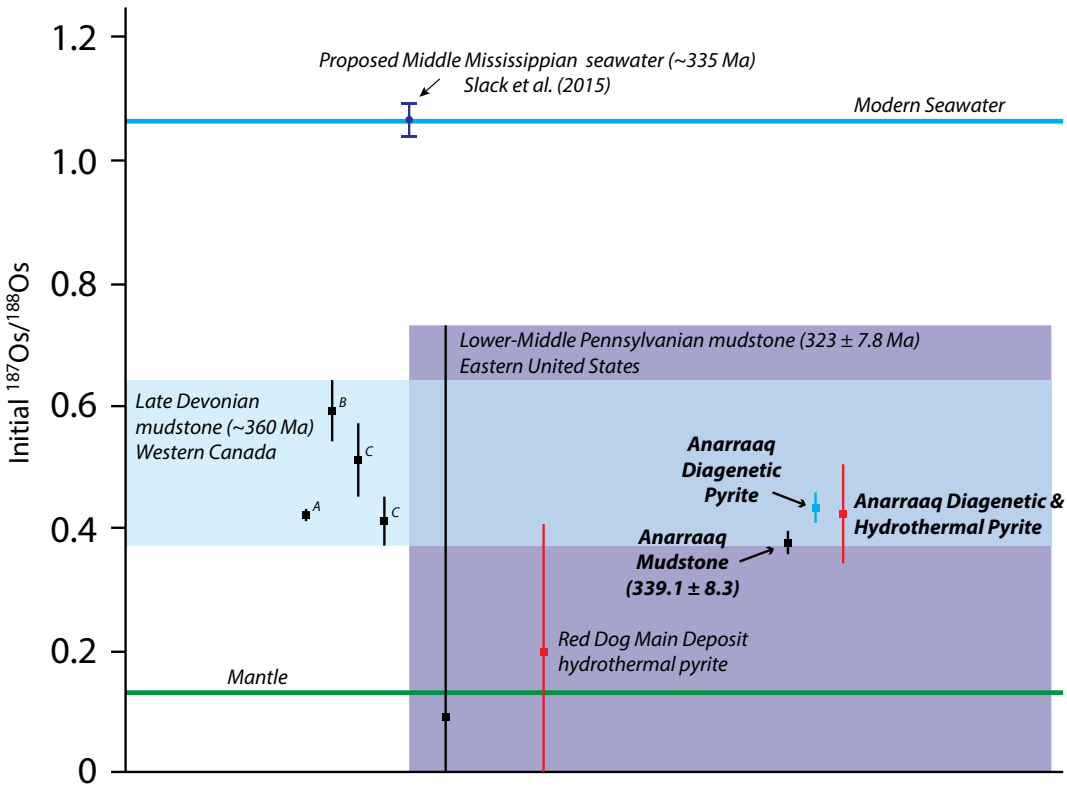

Fig. 14. Initial Os isotope composition ($^{187}Os/^{188}Os$) of diagenetic and hydrothermal pyrite from the Anarraaq sulfide deposit and overlying Ikalukrok mudstone. Also plotted are data from hydrothermal pyrite in the Red Dog Main deposit (Morelli et al., 2004), several Late Devonian mudstones (A: Selby and Creaser, 2005; B: Creaser et al., 2002; C: Selby and Creaser, 2003), and a Lower-Middle Pennsylvanian mudstone (Geboy et al., 2015). The Os compositions of modern seawater and the mantle reservoirs are from Peuckler-Ehrenbrink and Ravizza (2000).

Downloaded from http://pubs.geoscienceworld.org/segweb/economicgeology/article-pdf/116/8/1803/5428899/4849_reynolds_et_al.pdf
by Freie Universitaet Berlin user

not rule out local effects, especially if Ikalukrok mudstone was deposited in a restricted basin. We suggest that the variability in calculated initial $^{187}Os/^{188}Os$ values reported by Slack et al. (2015) was caused by postdepositional disturbance of the Re-Os system or the local contribution of a more radiogenic clastic component.

The initial $^{187}Os/^{188}Os$ value of the Anarraaq diagenetic pyrite isochron (0.432 ± 0.025) is only slightly higher than that of the mudstone (0.375 ± 0.019). We interpret diagenetic pyrite to have formed at an SMT during early diagenesis upon mixing of pore waters originally derived from Mississippian seawater. The similar initial $^{187}Os/^{188}Os$ values of diagenetic pyrite and mudstone are consistent with this interpretation.

The initial $^{187}Os/^{188}Os$ values reported in this study are within error of the value reported by Morelli et al. (2004) for hydrothermal pyrite in the Main deposit (0.2 ± 0.21; Fig. 14). However, our results are more precise and overlap only the highest part of the 2σ confidence range of Morelli et al. (2004). Because of the large uncertainty on the initial $^{187}Os/^{188}Os$ value, Morelli et al. (2004) considered both mantle and relatively young (<410 Ma) crustal reservoirs as possible sources of Os in the hydrothermal fluid. In view of the similarity between the initial $^{187}Os/^{188}Os$ of the mudstone isochron and the hydrothermal pyrite (regressed with diagenetic pyrite) at Anarraaq, influence from a mantle Os reservoir on the hydrothermal fluid composition is not required. In fact, the data from this study are compatible with the model of Leach et al. (2004), whereby hydrothermal fluids formed from a basinal brine evolved from evaporated seawater of Mississippian or Devonian age that circulated through the Devonian Endicott Group sedimentary rocks.

Implications for the genesis of, and exploration for, CD deposits

Evidence for early barite overprinted by zinc mineralization has been reported in the Main, Aqqaluk, Paalaaq, and Qanaiyaq deposits in the mine area (Kelley et al., 2004a; Blevings et al., 2013). As the Anarraaq sulfide deposit illustrates, barite can be poorly preserved and very difficult to identify: the deposit was discovered in 1999 (Kelley et al., 2004b), but only in this study do we show that barite was a significant component of the host rock, which has been almost totally replaced in the sulfide deposit. So, although several additional base metal deposits and prospects in the Red Dog district (e.g., Aktigiruk, Su Lik) reportedly contain no barite (Blevings et al., 2013), it is possible that barite was present initially but was then later replaced by hydrothermal minerals. Furthermore, we have suggested that at Anarraaq diagenetic pyrite and carbonate are also products of SD-AOM and are genetically linked to barite formation. Therefore, the presence of authigenic carbonate or laminated pyrite even in the absence of barite may reflect methane-driven diagenetic alteration, rather than hydrothermal processes.

Johnson et al. (2004) speculated that SD-AOM may have been the key chemical pathway for producing bisulfide for massive sulfide deposits at Red Dog, especially in deposits like Anarraaq where little to no diagenetic barite had been identified. The recognition that SD-AOM was an important diagenetic process at Anarraaq (Johnson et al., 2004; this study) is consistent with recent findings in other CD districts in the Canadian Cordillera. Magnall et al. (2016, 2020a, b) suggest that the CD Zn-Pb mineralization in the Tom and Jason deposits of Macmillan Pass (Yukon) overprints diagenetic barite and pyrite that formed at the SMT. Barite dissolution released sulfate and allows for sulfate cycling (Magnall et al., 2020b). Johnson et al. (2018) found that diagenetic pyrite and carbonate in the host strata of CD Zn-Pb mineralization at Howards Pass (Yukon-Northwest Territories) were also influenced by SD-AOM in the subsurface. All of these CD deposits, including those at Red Dog, are hosted in organic-rich sediment deposited on continental margins where upwelling of nutrient-rich deep ocean water resulted in abundant biological productivity in the water column (Dumoulin et al., 2014; Magnall et al., 2015, 2018, 2020b; Slack et al., 2017). At Howards Pass, Johnson et al. (2018) linked an increase in sedimentary carbon content to an increase in production of biogenic methane and influence of SD-AOM on diagenesis. It should be noted, however, that although SD-AOM produces sulfide, other reduction mechanisms such as bacterial and thermochemical sulfate reduction remain important processes and will also contribute reduced S to these large hydrothermal systems.

Magnall et al. (2020b) showed that the Ba released from barite dissolution at MacMillan Pass forms a halo of Ba enrichment in the host sediment around the sulfide bodies. In methane seeps, barium from dissolved barite can reprecipitate in younger strata (Brumsack, 1986; Torres et al., 1996, 2003). Barite is common in the younger Siksikpuk and Otuk Formations in the Red Dog plate (Young, 2004). Distinguishing relative Ba enrichment in the Ikalukrok or overlying units due to barite dissolution in zones of Zn-Pb mineralization could provide a useful vector for exploration. However, since the Anarraaq mineralized zones are fault bounded and the younger strata contain multiple repeating thrust sheets, it is not possible to test this hypothesis without a detailed structural reconstruction.

At Red Dog, the spatial coincidence between barite and overprinting Zn-Pb mineralization suggests a link between the mechanisms that control the location of methane-driven and hydrothermal alteration. One possibility is that early diagenetic and later hydrothermal fluids used similar pathways to flow into the shallow subsurface (Fig. 15). Diagenesis of biosiliceous mudstones has been linked with the development of nontectonic, intraformational faulting and pore fluid expulsion (Cartwright, 1994; Volpi et al., 2003; Davies et al., 2008), and this could have been the mechanism that controlled the location of large-scale SMT diagenesis. In the Red Dog district, hydrothermal fluids are thought to have flowed up extensional faults (Moore et al., 1986); these faults could have exploited preexisting faults or zones of weakness that served as flow pathways for diagenetic fluids bearing methane and barium. This interpretation would be consistent with the occurrence of some barite bodies that were not overprinted by hydrothermal fluids, as occur in the Red Dog district. This is important, as diagenetic barite creates gravity anomalies. Although these anomalies indicate the presence of prospective host rock, they are not directly linked to the existence of Zn-Pb mineralization.

According to the subclassification system of Cooke et al. (2000), stratiform CD Zn-Pb deposits are formed by either oxidized or reduced hydrothermal fluids. In this scheme, bar-

Downloaded from http://pubs.geoscienceworld.org/segweb/economicgeology/article-pdf/116/8/1803/5428899/4849_reynolds_et_al.pdf
by Freie Universitaet Berlin user

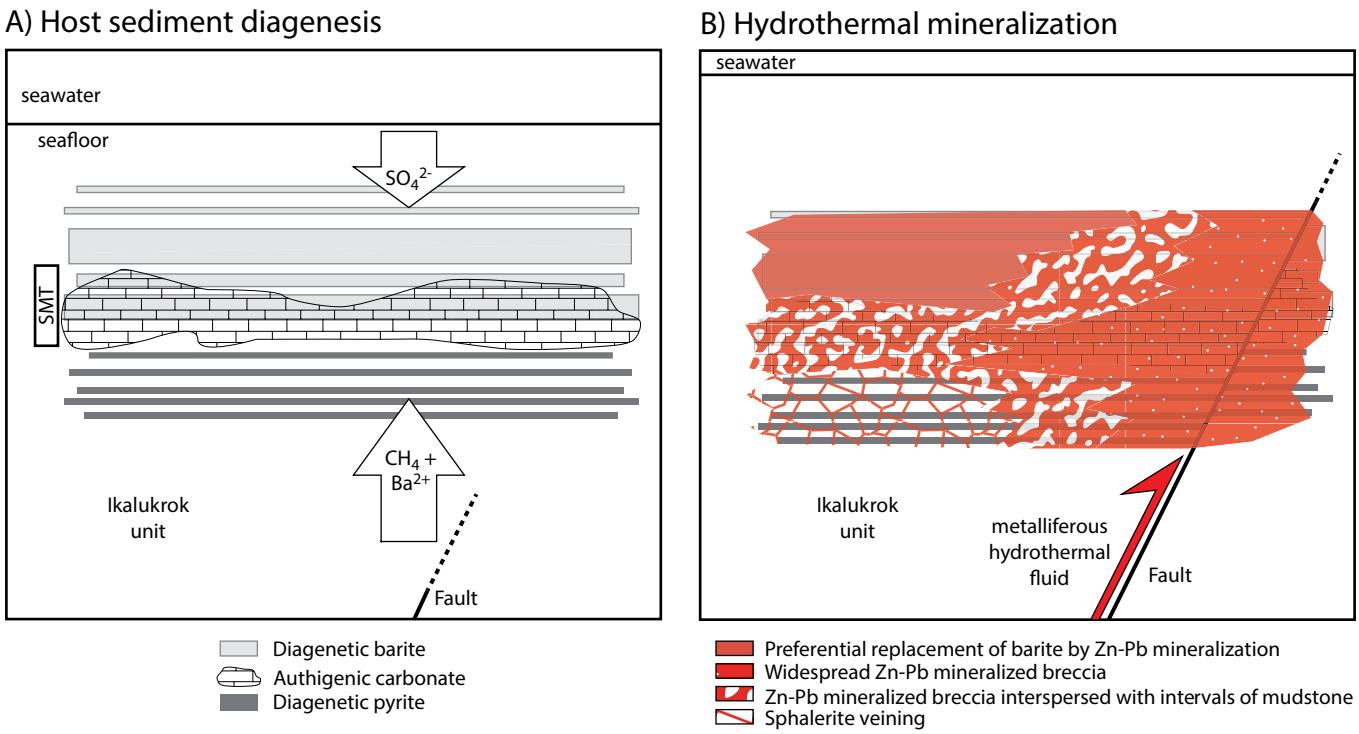

Fig. 15. Deposit model for the Anarraaq sulfide deposit. (A) Methanic and barium-rich diagenetic fluid interacts with seawater sulfate in pore waters to form diagenetic barite, carbonate, and pyrite. At least some dissolution of barite may take place as part of methane-driven diagenetic alteration. (B) Hydrothermal fluid dissolves authigenic and sedimentary carbonate, and possibly more barite, further increasing the porosity and permeability.

ite solubility is used as a boundary condition in the modeling of the chemistry of the hydrothermal fluid. This leads to the interpretation that these deposits formed from reduced fluids. However, as barite predates hydrothermal mineralization at Anarraaq (this study) and the Main deposits (Kelley et al., 2004a), its occurrence is independent of the composition of the hydrothermal fluid, and these fluids do not need to be reduced. At Macmillan Pass, Magnall et al. (2020b) show that hot (>300°C), carbonate-rich hydrothermal fluids resulted in the dissolution of barite and precipitation of barium carbonate minerals. Barium carbonates are not observed in the Anarraaq sulfide deposit (Kelley et al., 2004b; this study), which suggests a different mechanism drove barite dissolution. Barite is also soluble in hot (>200°C), strongly reducing fluids (Hanor, 2000). However, fluid inclusion microthermometry from the Main deposit suggests that hydrothermal fluids were 110°–180°C (Leach et al., 2004), and in this temperature range, barite has retrograde solubility (Bowers et al., 1984). An alternative explanation is that increasing temperatures associated with the onset of local hydrothermal activity resulted in the acceleration of diagenetic processes—a process that has been reported in modern methane seep settings (Guaymas basin; Einsele et al., 1980; Berndt et al., 2016) and inferred at Macmillan Pass (Magnall et al., 2020a). In the Anarraaq sulfide deposit, hydrothermal acceleration of diagenetic processes could explain the extensive dissolution of diagenetic barite and the formation of large volumes of diagenetic pyrite and potentially authigenic carbonate. Furthermore, pore water methane and/or the bisulfide produced by SD-AOM could have contributed to a trap for hydrothermal metals.

Based on logging and petrographic observations, we suggest that the dominant sulfide component of the northwestern, lower-grade part of the Anarraaq sulfide deposit is diagenetic pyrite. Previous workers (Kelley et al., 2004b; Schardt et al., 2008) have considered this zone to represent a hydrothermal pyrite halo. Instead, we consider the distal hydrothermal signature in this part of the deposit to be characterized by relatively minor sphalerite and Fe sulfide veining (Fig. 8I). Further study of the chemistry of these different pyrite generations will be necessary to assess if the chemical and isotopic composition of the diagenetic pyrite can be distinguished from the hydrothermal pyrite, as has been shown in other deposits (Large et al., 2009; Gadd et al., 2016; Magnall et al., 2020c).

In summary, understanding the mechanisms of formation of hydrothermal ore deposits that form in the shallow subsurface of marine sediment requires an understanding of key diagenetic processes. At Red Dog, diagenetic processes created physical and chemical traps for later Zn-Pb mineralization. These processes must be considered when developing an exploration program, and extra care must be taken to distinguish diagenetic and hydrothermal components during the interpretation of sedimentological, geochemical, and geophysical data.

Conclusions

The Anarraaq barite body contains barite, carbonate, and pyrite, which are interpreted to form in the subsurface by methane-driven diagenetic processes (i.e., at a paleo-SMT). New cross sections show that the Anarraaq sulfide deposit contains

Downloaded from http://pubs.geoscienceworld.org/segweb/economicgeology/article-pdf/116/8/1803/5428899/4849_reynolds_et_al.pdf
by Freie Universitaet Berlin user

two distinct zones of Zn-Pb mineralization (Upper and Lower), each of which contains evidence for a similar assemblage of diagenetic minerals. This suggests that hydrothermal mineralization overprinted paleo-SMTs. The presence of 10-cm quartz- and sulfide-infilled cavities in the Lower zone suggests that the host rock was mostly lithified before the onset of hydrothermal mineralization. Dissolution of barite and sedimentary and authigenic carbonate in the subsurface was an important permeability-generating process at Anarraaq. The cycle of barite precipitation and dissolution linked to the upward migration of an SMT over time may have introduced additional porosity and permeability to the host sediment prior to hydrothermal mineralization. Hydrothermal acceleration of diagenetic processes could explain the extensive dissolution of barite and the large volume of diagenetic pyrite and potentially authigenic carbonate present in the sulfide deposit. Furthermore, pore water methane and/or the bisulfide produced by SD-AOM could have contributed as a trap for metals transported by hydrothermal fluids.

The Re-Os isochron ages of Ikalukrok mudstone, diagenetic pyrite, and hydrothermal pyrite (isochron constructed in combination with diagenetic pyrite data) at Anarraaq are all within error of the Re-Os isochron age of the Main deposit in the Red Dog mine area (Morelli et al., 2004). This indicates that hydrothermal mineralizing events were broadly synchronous on a regional scale. The initial Os composition of the Anarraaq isochrons is consistent with expected values for Devonian and Mississippian seawater; it is unlikely that a mantle source had a significant influence on hydrothermal fluids.

Barite; pyrite layers, laminae, and nodules; textures suggestive of carbonate replacement; or some combination of these are reported in all known Red Dog deposits and prospects. This suggests that methane-driven diagenetic alteration was an important precondition for CD Zn-Pb mineralization in the Red Dog district. This idea is consistent with recent reports that SD-AOM was an important diagenetic process in sediments hosting CD deposits in Howard's Pass and MacMillan Pass. We propose that the size, mineralogy, and pore water composition of paleo-SMTs may have played a key role in ground preparation for forming large CD deposits.

Acknowledgments

This work was funded by Teck Resources Limited and by a Collaborative Research and Development grant and a Vanier Canada Graduate Scholarship from the Natural Sciences and Engineering Research Council of Canada. Special thanks to Pilar Lecumberri-Sanchez at the University of Alberta and Mo Snyder at Acadia University, and to the geologists active in the Red Dog district for technical assistance and geologic discussions. We acknowledge Gema Olivo for her early review of this manuscript and Elizabeth Turner, Karen Kelley, and Craig Johnson for their thorough reviews of this paper.

REFERENCES

Arning, E.T., Gaucher, E.C., van Berk, W., and Schulz, H.M., 2015, Hydrogeochemical models locating sulfate-methane transition zone in marine sediments overlying black shales: A new tool to locate biogenic methane?: Marine and Petroleum Geology, v. 59, p. 563–574, doi: 10.1016/j.marpetgeo.2014.10.004.

Ayuso, R.A., Kelley, K.D., Leach, D.L., Young, L.E., Slack, J.F., Wandlass, G., Lyon, A.M., and Dillingham, J.L., 2004, Origin of the Red Dog Zn-Pb-Ag deposits, Brooks Range, Alaska: Evidence from regional Pb and Sr isotope sources: Economic Geology, v. 99, p. 1533–1553, doi: 10.2113/gsecongeo.9.7.1533.

Barnes, R.O., and Goldberg, E.D., 1976, Methane production and consumption in anoxic marine sediments: Geology, May, p. 297–300, doi: 10.1130/0091-7613(1976)42.0.CO;2.

Berndt, C., Hensen, C., Mortera-Gutierrez, C., Sarkar, S., Geilert, S., Schmidt, M., Liebetrau, V., Kipfer, R., Scholz, F., Doll, M., and Muff, S., 2016, Rifting under steam: How rift magmatism triggers methane venting from sedimentary basins: Geology, v. 44, no. 9, p. 767–770.

Bishop, J.K.B., 1988, The barite-opal-organic carbon association in oceanic particulate matter: Nature, v. 332, p. 341–343, doi: 10.1038/332341a0.

Blevings, S., Kraft, J., Stemler, J., and Krolak, T., 2013, An overview of the structure, stratigraphy, and Zn-Pb-Ag deposits of the Red Dog district, northwestern Alaska: Society of Economic Geologists, Special Publication 17, p. 361–387.

Bowers, T.S., Jackson, K.J., and Helgeson, H.C., 1984, Equilibrium activity diagrams: Berlin, Springer-Verlag, p. 1–290.

Brumsack, H.J., 1986, The inorganic geochemistry of Cretaceous black shales (DSDP Leg 41) in comparison to modern upwelling sediments from the Gulf of California: Geological Society of London, Special Publication 21, p. 447–462, doi: 10.1144/GSL.SP.1986.021.01.30.

Burke, W.H., Denison, R.E., Hetherington, E.A., Koepnick, R.B., Nelson, H.F., and Otto, J.B., 1982, Variation of seawater Sr^{87}-Sr^{86} throughout Phanerozoic time: Geology, v. 10, p. 516–519, doi: 10.1130/0091-7613(1982)10<516:VOSSTP>2.0.CO.

Cartwright, J.A., 1994, Episodic basin-wide fluid expulsion from geopressured shale sequences in the North Sea basin: Geology, v. 22, p. 447–450, doi: 10.1130/0091-7613(1994)022<0447:EBWFEF>2.3.CO;2.

Cooke, D., Bull, S., Large, R., and McGoldrick, P., 2000, The importance of oxidized brines for the formation of Australian Proterozoic stratiform sediment-hosted Pb-Zn (Sedex) deposits: Economic Geology, v. 95, p. 1–18, doi: 10.2113/gsecongeo.95.1.1.

Creaser, R.A., Sannigrahi, P., Chacko, T., and Selby, D., 2002, Further evaluation of the Re-Os geochronometer in organic-rich sedimentary rocks: A test of hydrocarbon maturation effects in the Exshaw Formation, Western Canada sedimentary basin: Geochimica et Cosmochimica Acta, v. 66, p. 3441–3452, doi: 10.1016/S0016-7037(02)00939-0.

Davies, R.J., Goulty, N.R., and Meadows, D., 2008, Fluid flow due to the advance of basin-scale silica reaction zones: Bulletin of the Geological Society of America, v. 120, p. 195–206, doi: 10.1130/B26099.1.

Dean, W.E., and Schreiber, B.C., 1978, Authigenic barite: Leg 41 Deep Sea Drilling Project, v. 41, p. 915–931.

Denison, R.E., Koepnick, R.B., Burke, W.H., Hetherington, E.A., and Fletcher, A., 1994, Construction of the Mississippian, Pennsylvanian and Permian seawater $^{87}Sr/^{86}Sr$ curve: Chemical Geology: Isotope Geoscience Section, v. 112, p. 145–167.

De Vera, J., 2005, Structure of the Red Dog district, Western Brooks Range, Alaska: Ph.D. thesis, London, University of London, 633 p., www.arlis.org/docs/vol1/D/773627462.pdf.

De Vera, J., McClay, K., and King, A., 2004, Structure of the Red Dog district, Western Brooks Range, Alaska: Economic Geology, v. 99, p. 1415–1434, doi: 10.2113/gsecongeo.99.7.1415.

Dickens, G.R., 2001, Sulphate profiles and barium fronts in sediments on the Blake Ridge: Present and past methane fluxes through a large gas hydrate reservoir: Geochimica et Cosmochimica Acta, v. 65, p. 529–543.

Dumoulin, J.A., Harris, A.G., Blome, C.D., and Young, L.E., 2004, Depositional settings, correlation, and age of Carboniferous rocks in the western Brooks Range, Alaska: Economic Geology, v. 99, p. 1355–1384.

Dumoulin, J.A., Johnson, C.A., Slack, J.F., Bird, K.J., Whalen, M.T., Moore, T.E., Harris, A.G., and Sullivan, P.B.O., 2014, Carbonate margin, slope, and basin facies of the Lisburne Group (Carboniferous-Permian) in northern Alaska: Society of Sedimentary Geologists (SEPM), Special Publication 105, p. 211–236, doi: 10.2110/sepmsp.105.02.

Einsele, G., Gieskes, J.M., Curray, J., Moore, D.M., Aguayo, E., Aubry, M.-P., Fornari, D., Guerrero, J., Kastner, M., Kelts, K., Lyle, M., Matoba, Y., Molina-Cruz, A., Niemitz, J., et al., 1980, Intrusion of basaltic sills into highly porous sediments, and resulting hydrothermal activity: Nature, v. 283, p. 441–445.

Feng, D., and Roberts, H.H., 2011, Geochemical characteristics of the barite deposits at cold seeps from the northern Gulf of Mexico continental slope: Earth and Planetary Science Letters, v. 309, no. 1–2, p. 89–99.

Downloaded from http://pubs.geoscienceworld.org/segweb/economicgeology/article-pdf/116/8/1803/5428899/4849_reynolds_et_al.pdf
by Freie Universitaet Berlin user

Fernandes, N.A., Gleeson, S.A., Magnall, J.M., Creaser, R.A., Martel, E., Fischer, B.J., and Sharp, R., 2017, The origin of Late Devonian (Frasnian) stratiform and stratabound mudstone-hosted barite in the Selwyn basin, Northwest Territories, Canada: Marine and Petroleum Geology, v. 85, p. 1–15.

Gadd, M.G., Layton-Matthews, D., Peter, J.M., and Paradis, S.J., 2016, The world-class Howard's Pass SEDEX Zn-Pb district, Selwyn basin, Yukon. Part I: Trace element compositions of pyrite record input of hydrothermal, diagenetic, and metamorphic fluids to mineralization: Mineralium Deposita, v. 51, no. 3, p. 319–342.

Geboy, N.J., Tripathy, G.R., Ruppert, L.F., Eble, C.F., Blake, B.M., Hannah, J.L., and Stein, H.J., 2015, Re-Os age for the Lower-Middle Pennsylvanian boundary and comparison with associated palynoflora: International Journal of Coal Geology, v. 140, p. 23–30, doi: 10.1016/j.coal.2015.01.002.

Goodfellow, W.D., Lydon, J.W., and Turner, R.J., 1993, Geology and genesis of stratiform sediment-hosted (SEDEX) zinc-lead-silver sulphide deposits: Geological Association of Canada, Special Paper 40, p. 201–252.

Greinert, J., Bollwerk, S.M., Derkachev, A., Bohrmann, G., and Suess, E., 2002, Massive barite deposits and carbonate mineralization in the Derugin basin, Sea of Okhotsk: Precipitation processes at cold seep sites: Earth and Planetary Science Letters, v. 203, no. 1, p. 165–180.

Gwiazda, R.H., Paull, C.K., Caress, D., Preston, C.M., Lundsten, E., and Anderson, K., 2019, The extent of fault-associated modern authigenic barite deposits offshore northern Baja California revealed by high resolution mapping: Frontiers in Marine Science, v. 6, p. 460.

Hanor, J.S., 2000, Barite-celestine geochemistry and environments of formation: Reviews in Mineralogy and Geochemistry, v. 40, p. 193–275.

Hitzman, M.W., 1999, Routine staining of drill core to determine carbonate mineralogy and distinguish carbonate alteration textures: Mineralium Deposita, v. 34, no. 8, p. 794–798.

Hnatyshin, D., Kontak, D.J., Turner, E.C., Creaser, R.A., Morden, R., and Stern, R.A., 2016, Geochronologic (ReOs) and fluid-chemical constraints on the formation of the Mesoproterozoic-hosted Nanisivik ZnPb deposit, Nunavut, Canada: Evidence for early diagenetic, low-temperature conditions of formation: Ore Geology Reviews, v. 79, p. 189–217, doi: 10.1016/j.oregeorev.2016.05.017.

Hoehler, T.M., Alperin, M.J., Albert, D.B., and Martens, C.S., 1994, Field and laboratory studies of methane oxidation in an anoxic marine sediment: Evidence for a methanogen-sulfate reducer consortium: Global Biogeochemical Cycles, v. 8, p. 451–463, doi: 10.1029/94GB01800.

Isaacs, C.M., 1982, Influence of rock composition on kinetics of silica phase changes in the Monterey Formation, Santa Barbara area, California: Geology, v. 10, no. 6, p. 304–308.

Iversen, N., and Jørgensen, B.B., 1985, Anaerobic methane oxidation rates at the sulphate-methane transition in marine sediments from Kattegat and Skagerrak (Denmark): Limnology and Oceanography, v. 30, p. 944–955.

Johnson, C.A., Kelley, K.D., and Leach, D.L., 2004, Sulfur and oxygen isotopes in barite deposits of the western Brooks Range, Alaska, and implications for the origin of the Red Dog massive sulfide deposits: Economic Geology, v. 99, p. 1435–1448, doi: 10.2113/gsecongeo.99.7.1435.

Johnson, C.A., Emsbo, P., Poole, F.G., and Rye, R.O., 2009, Sulfur- and oxygen-isotopes in sediment-hosted stratiform barite deposits: Geochimica et Cosmochimica Acta, v. 73, p. 133–147, doi: 10.1016/j.gca.2008.10.011.

Johnson, C.A., Slack, J.F., Dumoulin, J.A., Kelley, K.D., and Falck, H., 2018, Sulfur isotopes of host strata for Howards Pass (Yukon-Northwest Territories) Zn-Pb deposits implicate anaerobic oxidation of methane, not basin stagnation: Geology, v. 46, p. 619–622, doi: 10.1130/G40274.1.

Jørgensen, B.B., Böttcher, M.E., Lüschen, H., Neretin, L.N., and Volkov, I.I., 2004, Anaerobic methane oxidation and a deep H_2S sink generate isotopically heavy sulfides in Black Sea sediments: Geochimica et Cosmochimica Acta, v. 68, p. 2095–2118, doi: 10.1016/j.gca.2003.07.017.

Kasten, S., Zabel, M., Heuer, V., and Hensen, C., 2003, Processes and signals of nonsteady-state diagenesis in deep-sea sediments and their pore waters, *in* Wefer, G., ed., The south Atlantic in the late Quaternary: Berlin, Heidelberg, Springer, p. 431–459.

Kelley, K.D., and Jennings, S., 2004, A special issue devoted to barite and Zn-Pb-Ag deposits in the Red Dog district, western Brooks Range, northern Alaska: Economic Geology, v. 99, no. 7, p. 1267–1280.

Kelley, K.D., Leach, D.L., Johnson, C.A., Clark, J.L., Fayek, M., Slack, J.F., Anderson, V.M., Ayuso, R.A., and Ridley, W.I., 2004a, Textural, compositional, and sulfur isotope variations of sulfide minerals in the Red Dog Zn-Pb-Ag deposits, Brooks Range, Alaska: Implications for ore formation: Economic Geology, v. 99, p. 1509–1532, doi: 10.2113/gsecongeo.99.7.1509.

Kelley, K.D., Dumoulin, J.A., and Jennings, S., 2004b, The Anarraaq Zn-Pb-Ag and barite deposit, northern Alaska: Evidence for replacement of carbonate by barite and sulfides: Economic Geology, v. 99, p. 1577–1591, doi: 10.2113/gsecongeo.99.7.1577.

Kendall, B., Creaser, R.A., Ross, G.M., and Selby, D., 2004, Constraints on the timing of Marinoan "Snowball Earth" glaciation by ^{187}Re-^{187}Os dating of a Neoproterozoic, post-glacial black shale in western Canada: Earth and Planetary Science Letters, v. 222, p. 729–740.

Knittel, K., and Boetius, A., 2009, Anaerobic oxidation of methane: Progress with an unknown process: Annual Review of Microbiology, v. 63, p. 311–334, doi: 10.1146/annurev.micro.61.080706.093130.

Krolak, T., Palmer, K., Lacouture, B., and Paley, N., 2017, Red Dog mine, Alaska, USA: Teck Resources Limited, NI 43-101 Technical Report, 143 p.

Large, R.R., Danyushevsky, L., Hollit, C., Maslennikov, V., Meffre, S., Gilbert, S., Bull, S., Scott, R., Emsbo, P., Thomas, H., Singh, B., and Foster, J., 2009, Gold and trace element zonation in pyrite using a laser imaging technique: Implications for the timing of gold in orogenic and Carlin-style sediment-hosted deposits: Economic Geology, v. 104, no. 5, p. 635–668.

Lash, G.G., 2015, Pyritization induced by anaerobic oxidation of methane (AOM): An example from the Upper Devonian shale succession, western New York, USA: Marine and Petroleum Geology, v. 68, p. 520–535, doi: 10.1016/j.marpetgeo.2015.10.002.

Leach, D.L., Marsh, E., Emsbo, P., Rombach, C.S., Kelley, K.D., and Anthony, M., 2004, Nature of hydrothermal fluids at the shale-hosted Red Dog Zn-Pb-Ag deposits, Brooks Range, Alaska: Economic Geology, v. 99, p. 1449–1480, doi: 10.2113/gsecongeo.99.7.1449.

Leach, D.L., Bradley, D.C., Huston, D., Pisarevsky, S.A., Taylor, R.D., and Gardoll, J., 2010, Sediment-hosted lead-zinc deposits in Earth history: Economic Geology, v. 105, p. 593–625.

Lin, Q., Wang, J., Algeo, T.J., Sun, F., and Lin, R., 2016, Enhanced framboidal pyrite formation related to anaerobic oxidation of methane in the sulfate-methane transition zone of the northern South China Sea: Marine Geology, v. 379, p. 100–108.

Lin, Z., Sun, X., Peckmann, J., Lu, Y., Xu, L., Strauss, H., Zhou, H., Gong, J., Lu, H., and Teichert, B.M.A., 2016, How sulfate-driven anaerobic oxidation of methane affects the sulfur isotopic composition of pyrite: A SIMS study from the South China Sea: Chemical Geology, v. 440, p. 26–41, doi: 10.1016/j.chemgeo.2016.07.007.

Ludwig, K., 2001, Isoplot 3.00, a geochronologic toolkit for Microsoft Excel: Berkeley Geochronological Center, Special Publication 4, p. 71.

Magnall, J.M., Gleeson, S.A., and Paradis, S., 2015, The importance of siliceous radiolarian-bearing mudstones in the formation of sediment-hosted Zn-Pb: Ba mineralization in the Selwyn basin, Yukon, Canada: Economic Geology, v. 110, p. 2139–2146.

Magnall, J.M., Gleeson, S.A., Stern, R.A., Newton, R.J., Poulton, S.W., and Paradis, S., 2016, Open system sulphate reduction in a diagenetic environment—isotopic analysis of barite ($\delta^{34}S$ and $\delta^{18}O$) and pyrite ($\delta^{34}S$) from the Tom and Jason Late Devonian Zn-Pb-Ba deposits, Selwyn basin, Canada: Geochimica et Cosmochimica Acta, doi: 10.1016/j.gca.2016.02.015.

Magnall, J.M., Gleeson, S.A., Poulton, S.W., Gordon, G.W., and Paradis, S., 2018, Links between seawater paleoredox and the formation of sediment-hosted massive sulphide (SHMS) deposits—Fe speciation and Mo isotope constraints from Late Devonian mudstones: Chemical Geology, v. 490, p. 45–60, doi: 10.1016/j.chemgeo.2018.05.005.

Magnall, J.M., Gleeson, S.A., and Paradis, S., 2020a, A new subseafloor replacement model for the MacMillan Pass clastic-dominant Zn-Pb ± Ba deposits (Yukon, Canada): Economic Geology, v. 115, p. 953–959.

Magnall, J.M., Gleeson, S.A., Creaser, R.A., Paradis, S., Glodny, J., and Kyle, J.R., 2020b, The mineralogical evolution of the clastic dominant (CD)-type Zn-Pb ± Ba deposits at Macmillan Pass (Yukon, Canada)—tracing subseafloor barite replacement in the layered mineralization: Economic Geology, v. 115, p. 961–979.

Magnall, J.M., Gleeson, S.A., Hayward, N., and Rocholl, A., 2020c, Massive sulfide Zn deposits in the Proterozoic did not require euxinia: Geochemical Perspectives Letters, v. 13, p. 19–24.

Moore, D.W., Young, L.E., Modene, J.S., and Plahuta, J.T., 1986, Geologic setting and genesis of the Red Dog zinc-lead-silver deposit, western Brooks Range, Alaska: Economic Geology, v. 81, p. 1696–1727, doi: 10.2113/gsecongeo.81.7.1696.

Moore, T.E., Wallace, W., Bird, K., Karl, S., Mull, C., and Dillon, J., 1994, Geology of northern Alaska, *in* Plafker, G., and Berg, H., eds., The geology of Alaska: Geological Society of America, Decade of North America Geology, v. G-1, p. 49–140.

Downloaded from http://pubs.geoscienceworld.org/segweb/economicgeology/article-pdf/116/8/1803/5428899/4849_reynolds_et_al.pdf
by Freie Universitaet Berlin user

Morelli, R.M., Creaser, R.A., Selby, D., Kelley, K.D., Leach, D.L., and King, A.R., 2004, Re-Os sulfide geochronology of the Red Dog sediment-hosted Zn-Pb-Ag deposit, Brooks Range, Alaska: Economic Geology, v. 99, p. 1569–1576, doi: 10.2113/gsecongeo.99.7.1569.

Paull, C.K., Chanton, J.P., Neumann, A.C., Coston, J.A., Martens, C.S., and Showers, W., 1992, Indicators of methane-derived carbonates and chemosynthetic organic carbon deposits: Examples from the Florida escarpment: Palaios, v. 7, p. 361–375, doi: 10.2307/3514822.

Paytan, A., Kastner, M., Martin, E.E., MacDougall, J.D., and Herbert, T., 1993, Marine barite as a monitor of seawater strontium isotope composition: Nature, v. 366, p. 445–449, doi: 10.1038/366445a0.

Peucker-Ehrenbrink, B., and Ravizza, G., 2000, The marine osmium isotope record: Terra Nova, v. 12, p. 205–219, doi: 10.1046/j.1365-3121.2000.00295.x.

Reeburgh, W.S., 1976, Methane consumption in Cariaco trench waters and sediments: Earth and Planetary Science Letters, v. 28, p. 337–344, doi: 10.1016/0012-821X(76)90195-3.

Reynolds, M.A., Gingras, M.K., Gleeson, S.A., and Stemler, J.U., 2015, More than a trace of oxygen: Ichnological constraints on the formation of the giant Zn-Pb-Ag ± Ba deposits, Red Dog district, Alaska: Geology, v. 43, doi: 10.1130/G36954.1.

Schardt, C., Garven, G., Kelley, K.D., and Leach, D.L., 2008, Reactive flow models of the Anarraaq Zn-Pb-Ag deposit, Red Dog district, Alaska: Mineralium Deposita, v. 43, p. 735–757, doi: 10.1007/s00126-008-0193-3.

Selby, D., and Creaser, R.A., 2003, Re-Os geochronology of organic rich sediments: An evaluation of organic matter analysis methods: Chemical Geology, v. 200, p. 225–240, doi: 10.1016/S0009-2541(03)00199-2.

——2005, Direct radiometric dating of the Devonian-Mississippian timescale boundary using the Re-Os black shale geochronometer: Geology, v. 33, p. 545–548, doi: 10.1130/G21324.1.

Slack, J.F., Dumoulin, J.A., Schmidt, J.M., Young, L.E., and Rombach, C.S., 2004, Paleozoic sedimentary rocks in the Red Dog Zn-Pb-Ag district and vicinity, western Brooks Range, Alaska: Provenance, deposition, and metallogenic significance: Economic Geology, v. 99, p. 1385–1414, doi: 10.2113/gsecongeo.99.7.1385.

Slack, J.F., Selby, D., and Dumoulin, J.A., 2015, Hydrothermal, biogenic, and seawater components in metalliferous black shales of the Brooks Range, Alaska: Synsedimentary metal enrichment in a carbonate ramp setting: Economic Geology, v. 110, p. 653–675, doi: 10.2113/econgeo.110.3.653.

Slack, J.F., Falck, H., Kelley, K.D., and Xue, G.G., 2017, Geochemistry of host rocks in the Howards Pass district, Yukon-Northwest Territories, Canada: Implications for sedimentary environments of Zn-Pb and phosphate mineralization: Mineralium Deposita, v. 52, p. 565–593.

Smoliar, M.I., Walker, R.J., and Morgan, J.W., 1996, Re-Os ages of group IIA, IIIA, IVA, and IVB iron meteorites: Science, v. 271, p. 1099–1102.

Snyder, G.T., Dickens, G.R., and Castellini, D.G., 2007, Labile barite contents and dissolved barium concentrations on Blake Ridge: New perspectives on barium cycling above gas hydrate systems: Journal of Geochemical Exploration, v. 95, p. 48–65, doi: 10.1016/j.gexplo.2007.06.001.

Suess, E., 2014, Marine cold seeps and their manifestations: Geological control, biogeochemical criteria and environmental conditions: International Journal of Earth Sciences, v. 103, p. 1889–1916, doi: 10.1007/s00531-014-1010-0.

Torres, M.E., Brumsack, H.J., Bohrmann, G., and Emeis, K.C., 1996, Barite fronts in continental margin sediments: A new look at barium remobilization in the zone of sulfate reduction and formation of heavy barites in diagenetic fronts: Chemical Geology, v. 127, p. 125–139, doi: 10.1016/0009-2541(95)00090-9.

Torres, M.E., Bohrmann, G., Dubé, T.E., and Poole, F.G., 2003, Formation of modern and Paleozoic stratiform barite at cold methane seeps on continental margins: Geology, v. 31, p. 897, doi: 10.1130/G19652.1.

Turekian, K.K., and Pegram, W.J., 1997, Os isotope record in a Cenozoic deep-sea core: Its relation to global tectonics and climate, *in* Ruddiman, W.F., ed., Tectonic uplift and climate change: Boston, Springer, p. 383–397, doi: 10.1007/978-1-4615-5935-1_17.

Veizer, J., Ala, D., Azmy, K., Bruckschen, P., Buhl, D., Bruhn, F., Garden, G.A.F., Diener, A., Ebneth, S., Godderis, Y., Jasper, T., Korte, C., Pawellek, F., Podlaha, O.G., et al., 1999, $^{87}Sr/^{86}Sr$, $\delta^{13}C$ and $\delta^{18}O$ evolution of Phanerozoic seawater: Chemical Geology, v. 161, p. 59–88, doi: 10.1016/S0009-2541(99)00081-9.

Volpi, V., Camerlenghi, A., Hillenbrand, C.-D., Rebescon, M., and Ivaldiz, R., 2003, Effects of biogenic silica on sediment compaction and slope stability on the Pacific margin of the Antarctic Peninsula: Basin Research, v. 15, p. 339–363, doi: 10.1046/j.1365-2117.2003.00210.x.

Wehrmann, L.M., Arndt, S., März, C., Ferdelman, T.G., and Brunner, B., 2013, The evolution of early diagenetic signals in Bering Sea subseafloor sediments in response to varying organic carbon deposition over the last 4.3 Ma: Geochimica et Cosmochimica Acta, v. 109, p. 175–196, doi: 10.1016/j.gca.2013.01.025.

Young, L.E., 2004, A geologic framework for mineralization in the Western Brooks Range, Alaska: Economic Geology, v. 99, p. 1281–1306, doi: 10.2113/gsecongeo.99.7.1281.

Merilie Reynolds is a mineral deposits geologist at the Northwest Territories Geological Survey (Canada). She received a B.A. degree in geology from Smith College in 2008 and a Ph.D. degree in earth and atmospheric sciences from the University of Alberta in 2019. Prior to starting graduate school, she worked for Barrick Gold Exploration in the Carlin gold camps of northern Nevada.

Downloaded from http://pubs.geoscienceworld.org/segweb/economicgeology/article-pdf/116/8/1803/5428899/4849_reynolds_et_al.pdf
by Freie Universitaet Berlin user